



**HAL**  
open science

# **Influence of increasing convergence obliquity and shallow slab geometry onto tectonic deformation and seismogenic behavior along the Northern Lesser Antilles zone**

Muriel Laurencin, D. Graindorge, F. Klingelhofer, B. Marcaillou, M. Evain

► **To cite this version:**

Muriel Laurencin, D. Graindorge, F. Klingelhofer, B. Marcaillou, M. Evain. Influence of increasing convergence obliquity and shallow slab geometry onto tectonic deformation and seismogenic behavior along the Northern Lesser Antilles zone. *Earth and Planetary Science Letters*, 2018, 492, pp.59 - 72. 10.1016/j.epsl.2018.03.048 . hal-01852728

**HAL Id: hal-01852728**

**<https://hal.science/hal-01852728>**

Submitted on 28 Nov 2021

**HAL** is a multi-disciplinary open access archive for the deposit and dissemination of scientific research documents, whether they are published or not. The documents may come from teaching and research institutions in France or abroad, or from public or private research centers.

L'archive ouverte pluridisciplinaire **HAL**, est destinée au dépôt et à la diffusion de documents scientifiques de niveau recherche, publiés ou non, émanant des établissements d'enseignement et de recherche français ou étrangers, des laboratoires publics ou privés.

# Influence of increasing convergence obliquity and shallow slab geometry onto tectonic deformation and seismogenic behavior along the Northern Lesser Antilles zone

Laurencin M.<sup>1</sup>; Graindorge D.<sup>1</sup>, Klingelhofer F.<sup>2</sup>, Marcaillou B.<sup>3</sup>, Evain M.<sup>2</sup>

<sup>1</sup>Geosciences Océan, UMR 6538, Université Bretagne Occidentale / Institut Universitaire Européen de la Mer, Place N. Copernic, 29280 Plouzané, France. <sup>2</sup>Ifremer, Brest, France.

<sup>3</sup>Université Côte d'Azur, CNRS, Observatoire de la Côte d'Azur, IRD, Géoazur, 250 Rue Albert Einstein, 06560 Valbonne, France.

Corresponding author: Muriel Laurencin ([muriel.laurencin@univ-brest.fr](mailto:muriel.laurencin@univ-brest.fr))

## Abstract

In subduction zones, the 3D geometry of the plate interface is one of the key parameters that controls margin tectonic deformation, interplate coupling and seismogenic behavior. The North American plate subducts beneath the convex Northern Lesser Antilles margin. This convergent plate boundary, with a northward increasing convergence obliquity, turns into a sinistral strike-slip limit at the northwestern end of the system. This geodynamic context suggests a complex slab geometry, which has never been imaged before. Moreover, the seismic activity and particularly the number of events with thrust focal mechanism compatible with subduction earthquakes, increases northward from the Barbuda-Anguilla segment to the Anguilla-Virgin Islands segment. One of the major questions in this area is thus to analyze the influence of the increasing convergence obliquity and the slab geometry onto tectonic deformation and seismogenic behavior of the subduction zone. Based on wide-angle and multichannel reflection seismic data acquired during the Antithesis cruises (2013-2016), we decipher the deep structure of this subduction zone. Velocity models derived from wide-angle data acquired across the Anegada Passage are consistent with the presence of a crust of oceanic affinity thickened by hotspot magmatism and probably affected by the Upper Cretaceous-Eocene arc magmatism forming the 'Great Arc of the Caribbean'. The slab is shallower beneath the Anguilla-Virgin Islands margin segment than beneath the Anguilla-Barbuda segment which is likely to be directly related to the convex geometry of the upper plate. This shallower slab is located under the forearc where earthquakes and partitioning deformations increase locally. Thus, the shallowing slab might result in local greater interplate coupling and basal friction favoring seismic activity and tectonic partitioning beneath the Virgin Islands platform.

**Keywords:** Northern Lesser Antilles subduction; crust nature; interplate geometry; partitioning; interplate coupling; seismic data

## 1. Introduction

In subduction zones, the downgoing plate dynamics directly influence the upper plate deformation and geological processes such as uplift and subsidence within forearc and backarc, strain partitioning in oblique subduction (e.g. McCaffrey 1992), location of the volcanic arc (e.g. Syracuse and Abers 2006), and seismogenic potential (e.g. McCann et al. 1979). At shallow depths (0-40-km), chemical reactions, fluid release within the subducting plate and upper plate nature can play a key role in behavior and geometry of the subduction interface (e.g. Barker et al. 2009 and references therein), such as in the Hikurangi interplate subduction (e.g.

43 Barker et al. 2009). Many plates subduct under a curved margin (as Scotia, Marianas, Northern  
44 Chilean, Aleutian subductions ...). At large scale (0-600-km-depth), curved deformation front  
45 are often related with slab complex 3D geometry proposed by modeling (e.g. Schellart et al.  
46 2007; Bonnardot et al. 2008) and observed in different real cases (e.g. Hayes et al. 2012).  
47 Subsequently, observed variations of nature and geometry of the subducting plate at shallower  
48 depths (< 40-km-depth) for curved margins can play a major role on subduction zone processes  
49 and upper plate deformation.

50 The northeast Caribbean margin is sharply curved with a NS-trending subduction line offshore  
51 of the Central Lesser Antilles progressively rotating northward to an E-W direction to the north  
52 of the Greater Antilles (Figures 1 and 2). On the one hand, the N254°E convergence direction  
53 does not change along-strike resulting in an arcuate slab with a westward dip beneath the  
54 Central Lesser Antilles and a southward dip beneath Puerto Rico and Hispaniola islands. On  
55 the other hand, the Lesser Antilles margin presents heterogeneities in seismicity (McCann and  
56 Sykes 1984) and partitioning (Laurencin et al. 2017) locations. The Antithesis 1 (11/2013-  
57 01/2014) and Antithesis 3 (05/2016) cruises were aimed at studying the deep structure and the  
58 tectonic deformation of the poorly investigated Northern Lesser Antilles margin (Barbuda-  
59 Virgin Islands). Subsequently, using combined wide-angle and deep multichannel seismic data,  
60 we investigated the geometry of the downgoing slab and the nature of the overriding crust in  
61 order to discuss its influence onto partitioning deformation and seismic coupling.

## 62 2. Geodynamical setting

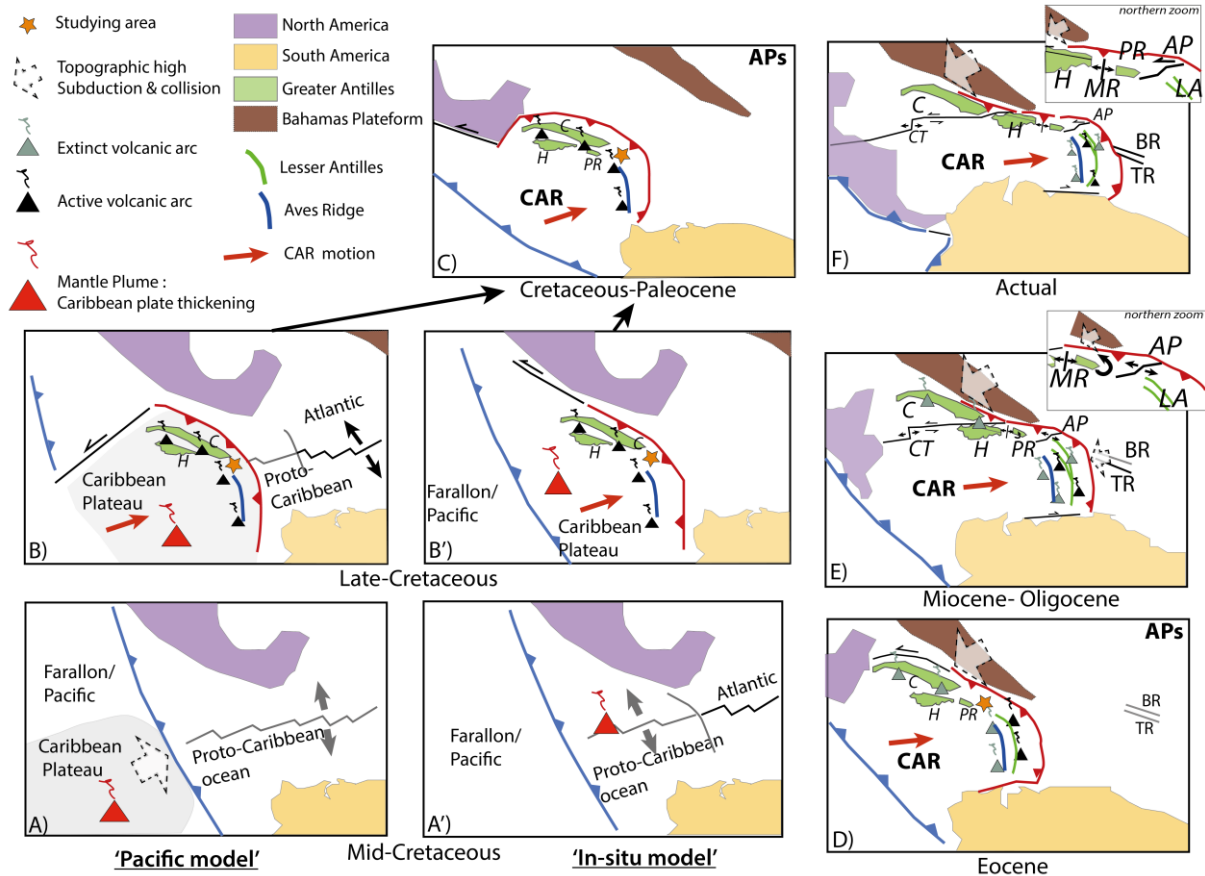
### 63 2.1. Nature and origin of the eastern Caribbean region

64 The eastern Caribbean plate, bounded by convergent margin from the southeast of Cuba to the  
65 south of the Lesser Antilles, includes an active island arc (Lesser Antilles arc) and a remnant  
66 arc, named the '*Great Arc of the Caribbean*' (currently the Greater Antilles and the Aves  
67 Ridge), setting up on the '*Caribbean Plateau*' (Figures 1 and 2). Two competing models depict  
68 the '*Caribbean Plateau*' formation. The '*Pacific*' model proposes an initiation of the  
69 '*Caribbean Plateau*' within the Pacific plate during Jurassic, thickened during the Cretaceous  
70 by magmatism above a mantle plume (Galapagos), (Figure 1-A-B), and later drifted to its  
71 present position between the two American plates (e.g. Pindell and Kennan 2009). On the  
72 contrary, the '*in situ*' model suggests that the thickening by decompression melting during Mid-  
73 Cretaceous of the '*Proto-Caribbean*' oceanic crust, forms the '*Caribbean Plateau*' (Meschede  
74 and Frisch 1998; James 2009), (Figure 1-A'-B').

75 The subduction of Atlantic lithosphere beneath the Caribbean plate since at least Cretaceous to  
76 Eocene times forms the '*Great Arc of the Caribbean*'. Fragments of this volcanic arc can be  
77 found in the residual Greater Antilles islands for Aptian times and in Puerto Rico for mid-  
78 Eocene times (Jolly et al. 2008; Boschman et al. 2014), (Figure 1-AB-A'B'-C).

79 During the Eocene (Figure 1-D), the arc volcanism likely migrated eastward from the Aves  
80 Ridge to the Lesser Antilles arc caused by the collision of the Bahamas on the northern  
81 Caribbean margin (Bouysse et al. 1985; Neill et al. 2011), (Figure 1-D). This Lesser Antilles  
82 arc was active from Eocene to Oligocene (Bouysse and Westercamp 1990). During the  
83 Oligocene (Figure 1-E), the Lesser Antilles arc moved westward to its current position possibly  
84 due to slab flattening or in response to the subduction of the Barracuda and Tiburon ridges in  
85 the Central Antilles (Bouysse and Westercamp 1990).

86 Wide-angle seismic data acquired in the Central (Kopp et al. 2011) and Southern Lesser Antilles  
 87 (Christeson et al. 2008) image a 25-km-thick crust which is interpreted as being of oceanic  
 88 affinity thickened by magmatism, coincident with the first steps of both geodynamic models.  
 89 Moreover, Christeson et al. (2008) conclude that the subduction magmatism forming the ‘Great  
 90 Arc of the Caribbean’ and that of the Lesser Antilles are comparable and do not imply variations  
 91 in crustal velocities. Finally, the volcanism forming the ‘Great Arc of the Caribbean’ and the  
 92 Lesser Antilles arc has a very low production rate and a local magmatic extension (Christeson  
 93 et al. 2008; Kopp et al. 2011).



94 *Figure 1: Two alternate geodynamic reconstructions for the Caribbean Plate since Mid-Cretaceous:*  
 95 *the ‘Pacific model’ (A-B) from Pindell and Kennan (2009) and Boschman et al. (2014), the ‘in-situ’*  
 96 *model (A’B’) from Meschede and Frisch (1998) and James (2009). These reconstructions include (C-*  
 97 *D) the collision of the Bahamas Bank, (E) the westward migration of the Lesser Antilles volcanic arc*  
 98 *(Bouysse and Westercamp, 1990); the rotation of Puerto Rico-Virgin Islands bloc (Reid et al., 1991);*  
 99 *the Mona rift and Anegada Passage opening (P. Mann et al. 2005; Laurencin et al. 2017) and (F) the*  
 100 *current tectonic partitioning (Laurencin et al., 2017). AP: Anegada Passage; APs: American plates;*  
 101 *BR: Barracuda Ridge; C: Cuba; CAR: Caribbean plate; CT: Cayman Trough; H: Hispaniola; MR:*  
 102 *Mona rift; PR: Puerto Rico; TR: Tiburon Ridge*

## 103 2.2. The Northern Lesser Antilles regional setting

104 The North American plate subducts below the Caribbean plate with a convergence rate of 20  
 105 mm/y in a N254°E direction (DeMets et al. 2000), (Figure 1-F). The convexity of the eastern  
 106 part of the Caribbean plate implies a subduction obliquity less than 30° to the south of Barbuda  
 107 and increasing northward to ~72° to the north of Puerto Rico (Figure 2).

108 Partitioning of the tectonic deformation is frequent within margins that undergo oblique plate  
 109 convergence (e.g. Fitch 1972). At the Northern Lesser Antilles subduction zone, the strain

110 partitioning is possibly accommodated by 1) a ~600 x 250 km northward migrating sliver  
111 bounded by a major sinistral strike-slip system in the volcanic arc (López et al. 2006), or 2) arc-  
112 perpendicular grabens bounded by ENE-WSW-trending normal faults (Feuillet et al. 2011).  
113 Both interpretations suggest a total partitioning of the forearc. These models are still highly  
114 debated. A recent interpretation of the first deep seismic data ever recorded in the Northern  
115 Lesser Antilles indicates that 1) the 850-km-long sinistral strike-slip Bunce fault (Ten Brink et  
116 al. 2004) located in the frontal part of the margin, extends as far south as offshore Barbuda  
117 island (Laurencin et al. 2017) and 2) the inherited 450-km-long left-lateral strike-slip system  
118 named Anegada Passage extends through the arc and the forearc from southeast of Puerto Rico  
119 to the Bunce fault (Laurencin et al. 2017), (Figure 2).

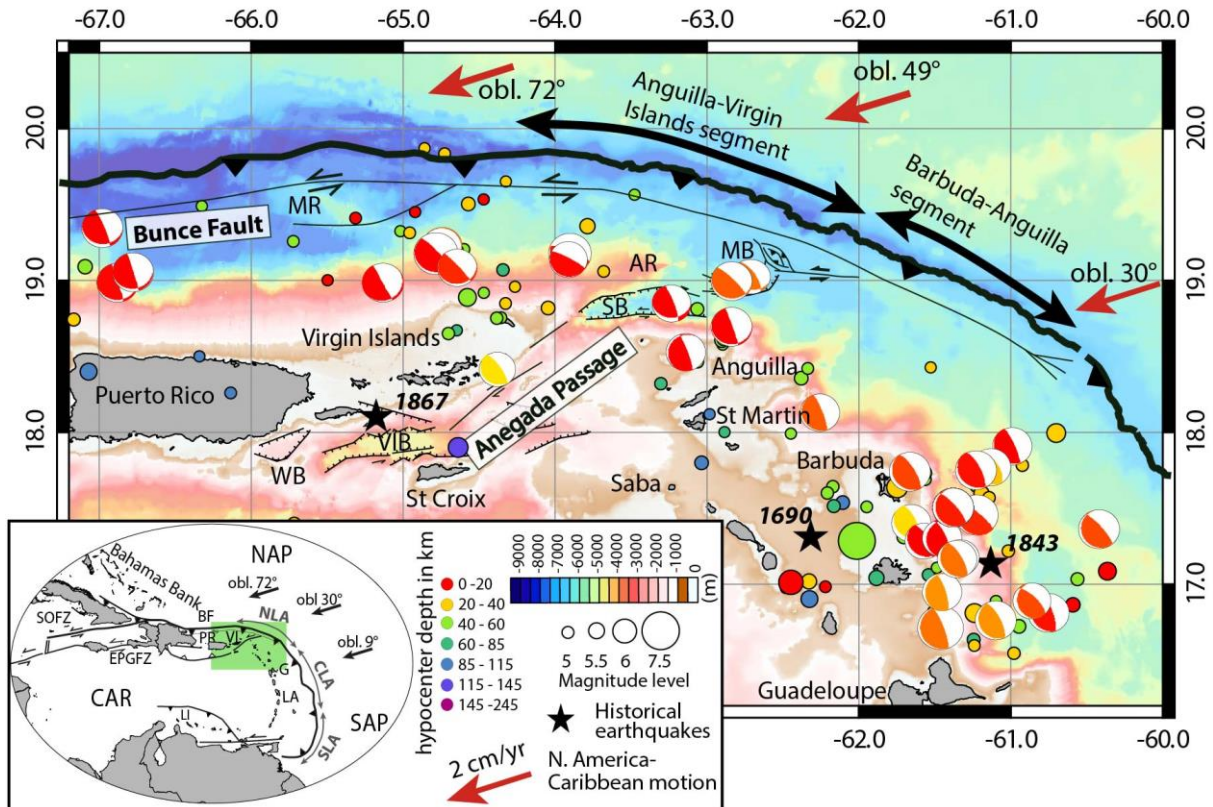
120 Hypocenter locations (McCann and Sykes 1984) and earthquake tomography (e.g. Van  
121 Benthem et al. 2013) suggest a complex shape for this arcuate slab where it plunges toward the  
122 south, north of Hispaniola-Puerto Rico and toward the west at the Central Lesser Antilles. In  
123 the Northern Lesser Antilles, it possibly includes local dip angle variations accommodated by  
124 a tear fault near Puerto Rico (Ten Brink 2005; Meighan et al. 2013).

125 The recent seismicity is heterogeneous in the Lesser Antilles region. The number of shallow,  
126 0-40-km-depth, earthquakes (PDE/NEIC catalog,  $M_w > 5$ , since 1900) and thrust focal  
127 mechanism earthquakes (CMT database: <http://www.globalcmt.org>,  $M_w > 3$ , since 1976) is low  
128 along the Barbuda-Anguilla segment. This seismicity increases south of Barbuda toward the  
129 Central Lesser Antilles and northward in the Anguilla-Virgin Islands segment (Figure 2). Three  
130 historical earthquakes were recorded in the Northern Lesser Antilles: 1690, 1843, 1867  
131 (Bernard and Lambert 1988; Feuillet et al. 2011), (Figure 2). But, only one event, the 1843  
132 earthquake ( $M > 8.5$ ) is possibly interpreted as a great subduction earthquake (Bernard and  
133 Lambert 1988; Feuillet et al. 2011). This heterogeneous distribution draws a seismic gap from  
134 Barbuda to Anguilla islands that previous studies already pointed out (e.g. McCann and Sykes  
135 1984). This gap is either temporal or related to long-term variations in interplate seismic  
136 coupling (e.g. Smithe et al. 2015).

137 Based on GPS data, Manaker et al. (2008) and Smithe et al. (2015) propose a very low  
138 coupling along the Lesser Antilles and Puerto Rico subduction interface resulting in an poorly  
139 coupled margin or in a 2000-years-long seismic cycle.

140

141



142

143 *Figure 2: Seismicity along the Lesser Antilles margin. The colored circles are the epicenters and the*  
 144 *beach-balls represent the focal mechanism from PDE/NEIC catalog with size and color representing*  
 145 *magnitude and hypocentral depth. Subduction focal mechanisms from Global CMT Catalog and colors*  
 146 *represents the depth. Tectonic features are from Jany et al. (1990); ten Brink et al. (2004); Laurencin*  
 147 *et al. (2017). The black stars represent three historical earthquakes. The red arrows correspond to*  
 148 *convergence vector between North American and the Caribbean Plates (DeMets et al. 2000). AR:*  
 149 *Anegada Ridge; BF: Bunce Fault; MB: Malliwana Basin; MR: Main Ridge; SB: Sombrero Basin; VIB:*  
 150 *Virgin Islands Basin; WB: Whiting Basin. Bottom left inset displays larger tectonic setting with position*  
 151 *of Northern Lesser Antilles (NAP), Central Lesser Antilles (CLA) and Southern Lesser Antilles (SLA).*  
 152 *CAR: Caribbean Plate; EPGFZ: Enriquillo-Plantain Garden Fault Zone; G: Guadeloupe; LA: Lesser*  
 153 *Antilles; LI: Leeward Islands; NAP: North American Plate; PR: Puerto Rico; SAP: South American*  
 154 *Plate; SOFZ: Septentrional-Oriente Fault Zone; VI: Virgin Islands.*

## 155 3. Data Acquisition and Processing

### 156 3.1. Data Acquisition

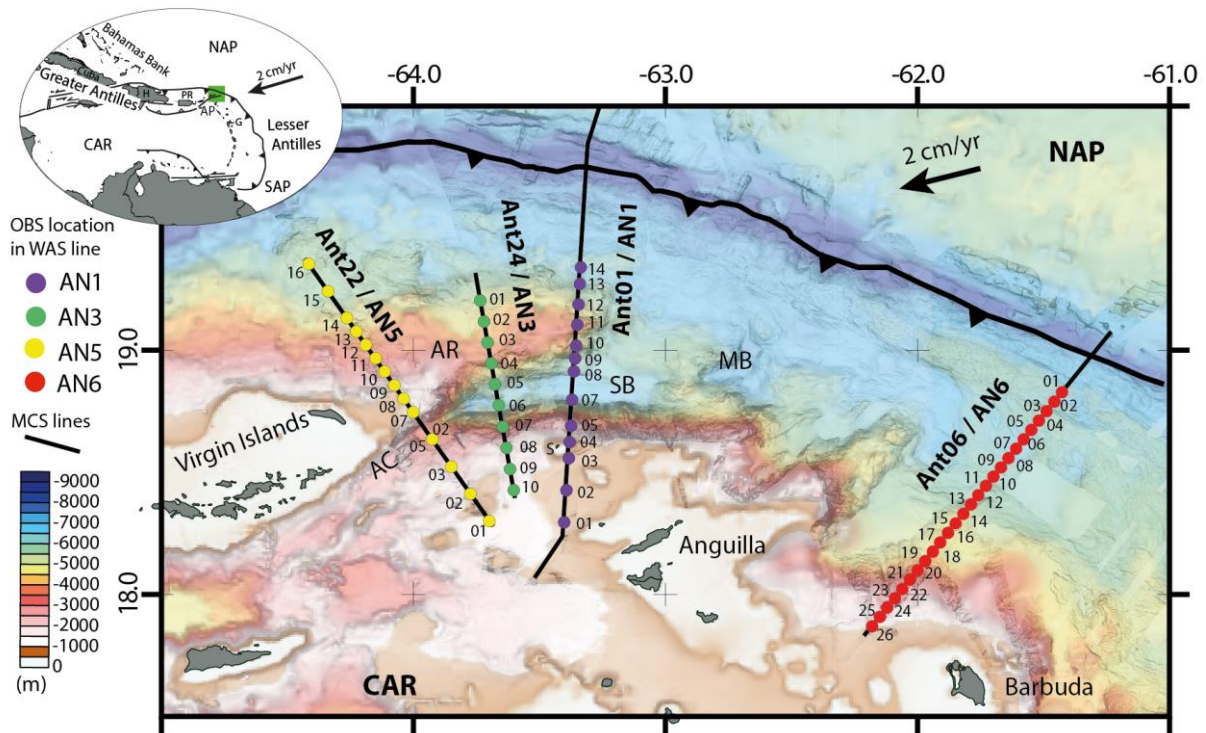


Figure 3: Location of Ocean Bottom Seismometers (colored circle), wide-angle and multichannel reflection seismic lines (solid line) recorded during the Antithesis cruise (Marcaillou and Klingelhoefer 2013). Top left inset displays larger tectonic setting. A: Anguilla, AC: Anegada Canyon, AR: Anegada Ridge; G: Guadeloupe, MB: Malliwana Basin, SB: Sombrero Basin, CAR: Caribbean Plate, NAP: North American Plate, SAP: South American Plate.

157 During the cruises Antithesis 1 and 3, four combined multichannel (MCS) and wide-angle  
158 seismic (WAS) lines were acquired along with multibeam bathymetric data (Figure 3). We  
159 recorded WAS data along lines AN1, AN3, AN5 and AN6, onboard R/V *L'Atalante*, with a 126  
160 L (7699 in<sup>3</sup>) airgun array, and 40 ocean-bottom seismometers (OBS) from the Ifremer/UBO  
161 pool. The OBS include a three component 4.5 Hz geophone and one 3 Hz hydrophone (Auffret  
162 et al. 2004). We acquired MCS lines Ant01 and Ant06, which correspond to wide-angle lines  
163 AN1 and AN6, during cruise Antithesis 1 with a 3.75-km-long 300-channels streamer. We  
164 acquired MCS lines Ant22 and Ant24, which correspond to wide-angle lines AN3 and AN5,  
165 during cruise Antithesis 3 onboard R/V *Pourquoi Pas?*, using a 106 L (6500 in<sup>3</sup>) airgun array  
166 and a 4.5-km-long 720-channels streamer. The combined WAS and MCS lines AN1/Ant01,  
167 AN3/Ant24 and AN5/Ant22 image the structure of the Anguilla-Virgin Islands segment and  
168 line AN6/Ant06 visualizes the depth structure between Barbuda and Anguilla.

### 169 3.2. Pre-processing of wide-angle seismic data

170 The OBS data pre-processing includes the correction for clock drifts and the instrument  
171 relocation for spatial drift using the water wave arrival and shot geometry. The mean horizontal  
172 drift compared to the deployment position during the diving period is 185 m and up-to ~600 m.  
173 In order to increase signal-to-noise ratio and facilitate the identification of far offset arrivals,

174 several processing steps were applied on the OBS data including: band-pass filtering,  
175 deconvolution and automatic gain control (Figure 4).

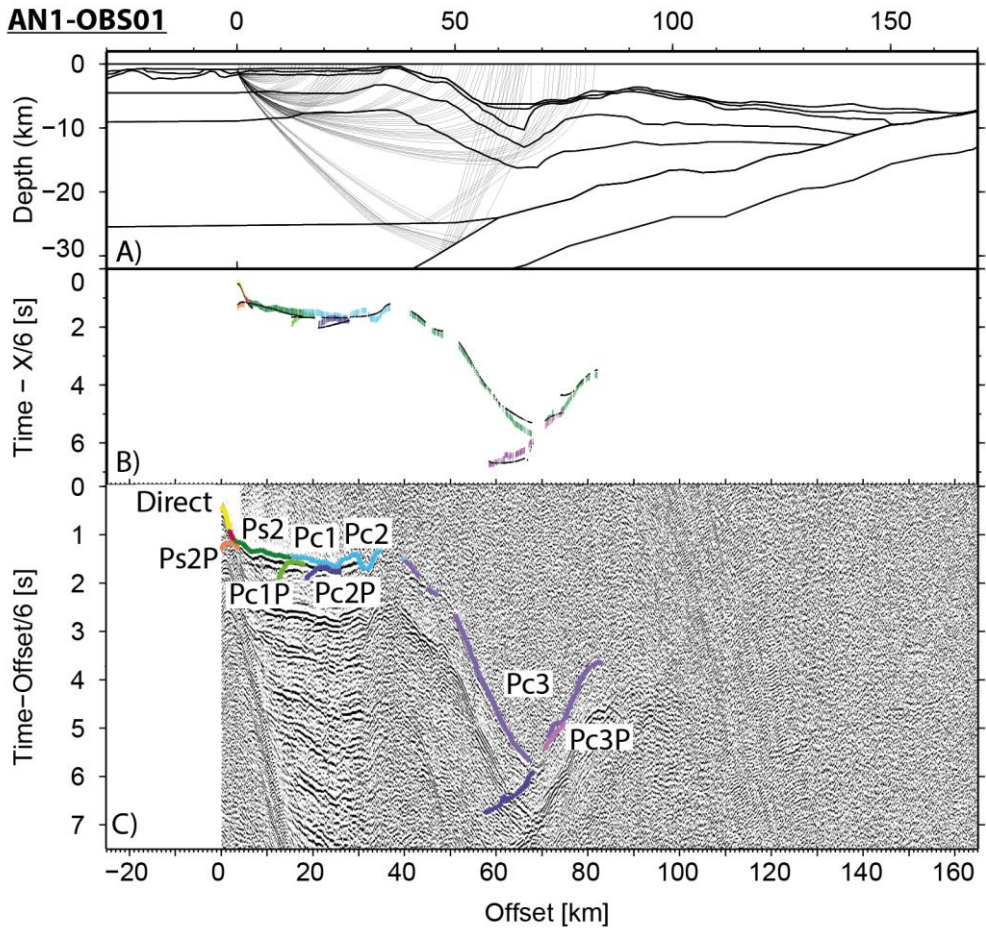
### 176 3.3. Velocity modelling profiles

#### 177 3.3.1. Method and WAG modeling

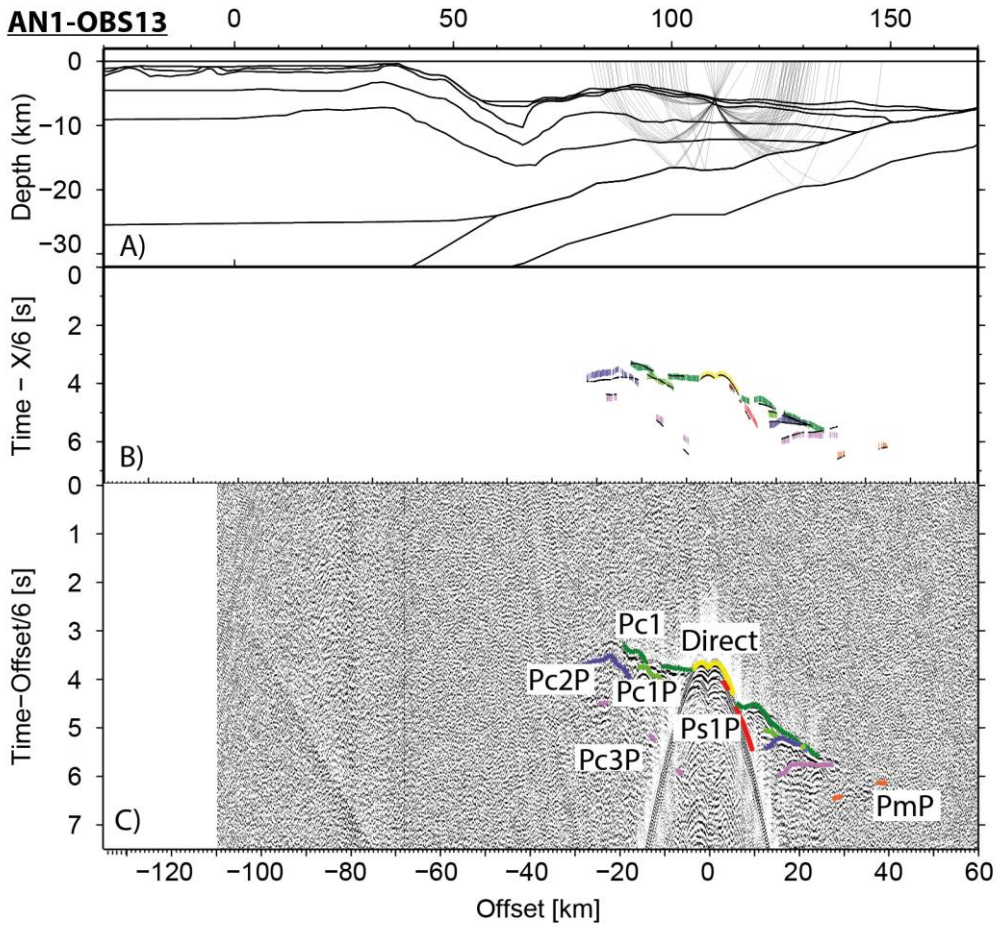
178 The forward modelling consists of 2D ray tracing within a determined velocity-depth model to  
179 reduce the misfit between observed and calculated travel-times of both refracted and reflected  
180 arrivals (Zelt and Smith 1992). Models are built from top to bottom following a layer-stripping  
181 approach with interfaces defined by velocity and depth nodes. Refracted and reflected arrivals  
182 picking was done using the different unfiltered and filtered record sections on both hydrophone  
183 and geophones components.

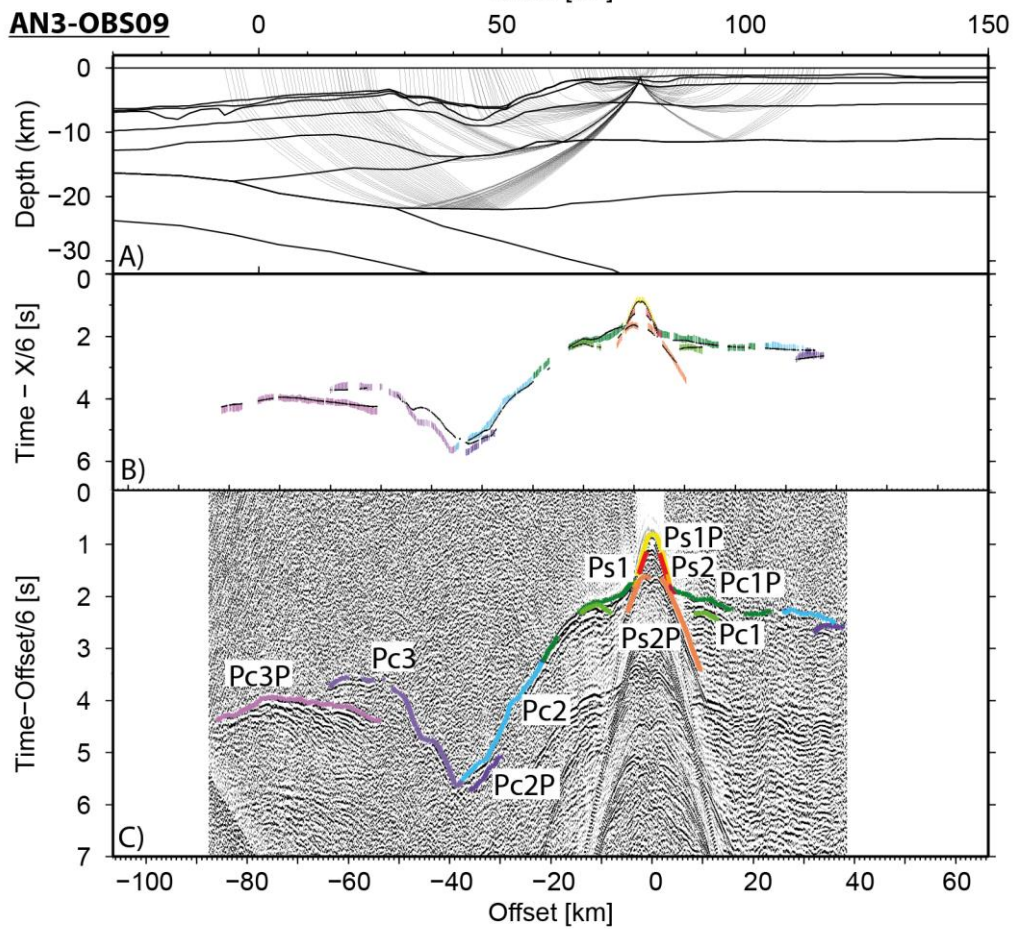
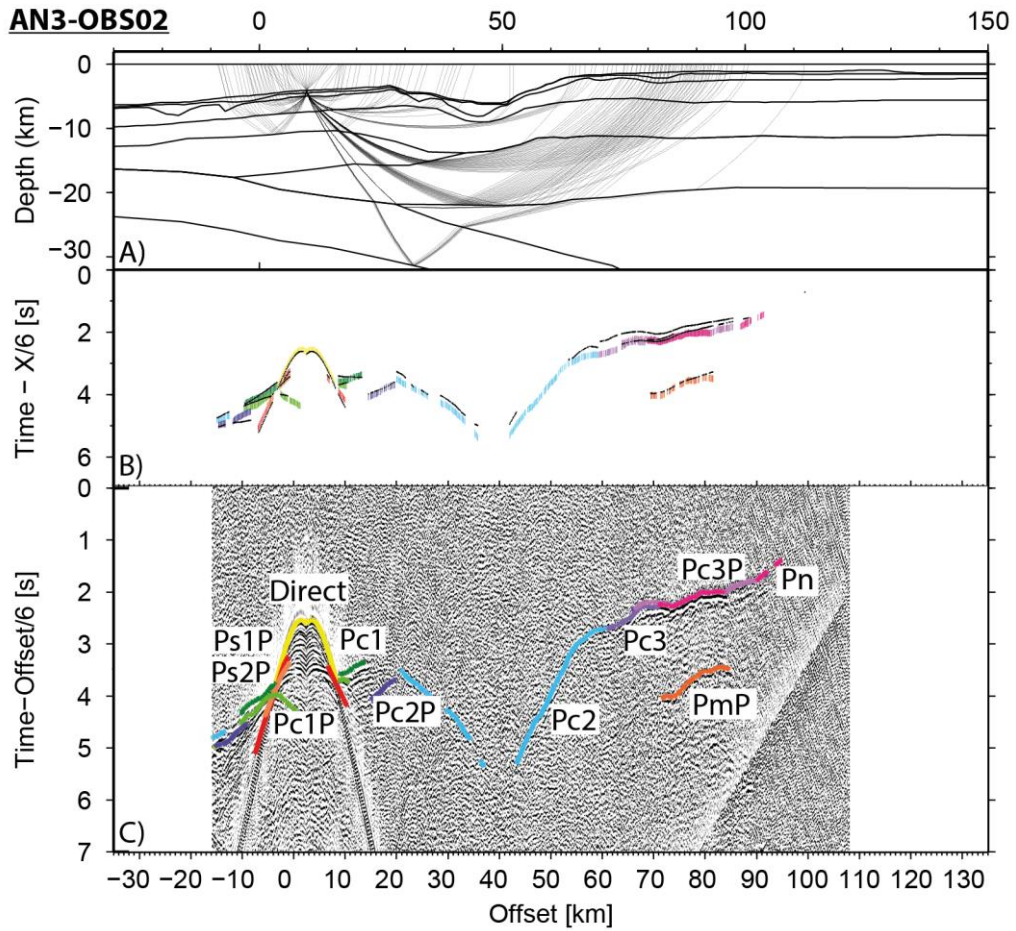
184 The Figure 4 displays 6 interpreted OBS sections (2 per wide-angle lines), additional OBS  
185 sections with and without interpretation are shown in the supplementary data. Models include  
186 two to four sedimentary layers determined using reflected (Ps1 to Ps4) and refracted (Ps1P to  
187 Ps4P) phases (Figure 4). Picking the sedimentary interfaces along the coincident MCS lines  
188 helps to constrain geometries of the sedimentary layers for the wide-angle models (seismic pre-  
189 processing and processing in Laurencin et al. (2017) and in supplementary material). The P-  
190 wave velocity derived from OBS data allows the depth conversion of the picked interfaces. We  
191 used refracted (Pc1, Pc2, Pc3, Pc4) and reflected (Pc1P, Pc2P, Pc3P, Pc4P) phases of wide-  
192 angle data to define the three or four crustal layers (Figure 4). The reflected arrivals on the  
193 upper mantle of the upper plate (Pc4P) are clear, but the velocities at depth are poorly  
194 constrained because of the scarcity of refracted arrivals in the mantle wedge (Pn) (Figure 4).  
195 The top of the oceanic plate is generally better constrained by wide angle reflected arrivals  
196 (Pc4P) (Figure 4) and by interpretation of coincident MCS lines. No clear turning ray arrivals  
197 from the subducting oceanic plate were identified, and only few reflected phases from its base  
198 could be picked (PmP) (Figure 4). Thus, the velocity and the thickness of the oceanic plate are  
199 relatively poorly constrained by the velocity modeling only. Beneath the Sombrero Basin along  
200 the lines AN1 and AN3 (Figure 5-A), despite the fact that some arrivals are identifiable, it was  
201 impossible to adjust a definitive model (numerical instability of the code when calculating ray  
202 paths in complex structures) because of a high lateral variability of the structure within the  
203 Anegada Passage.

**AN1-OBS01**



**AN1-OBS13**





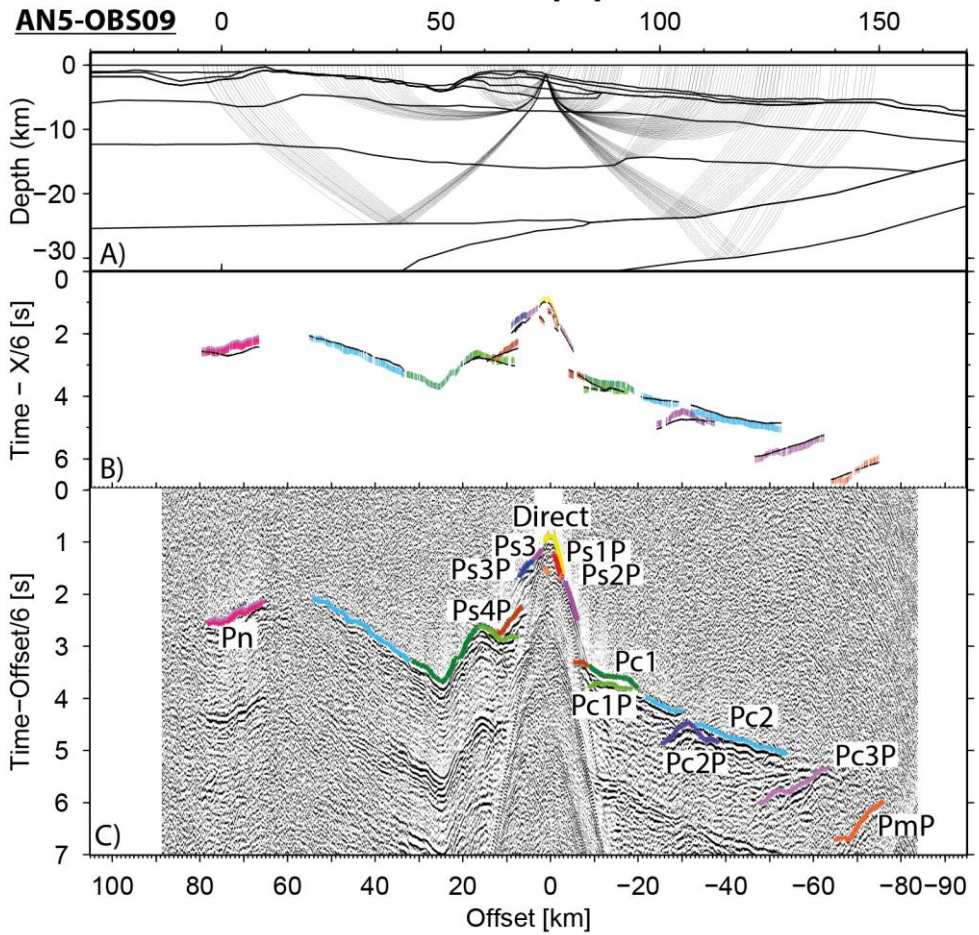
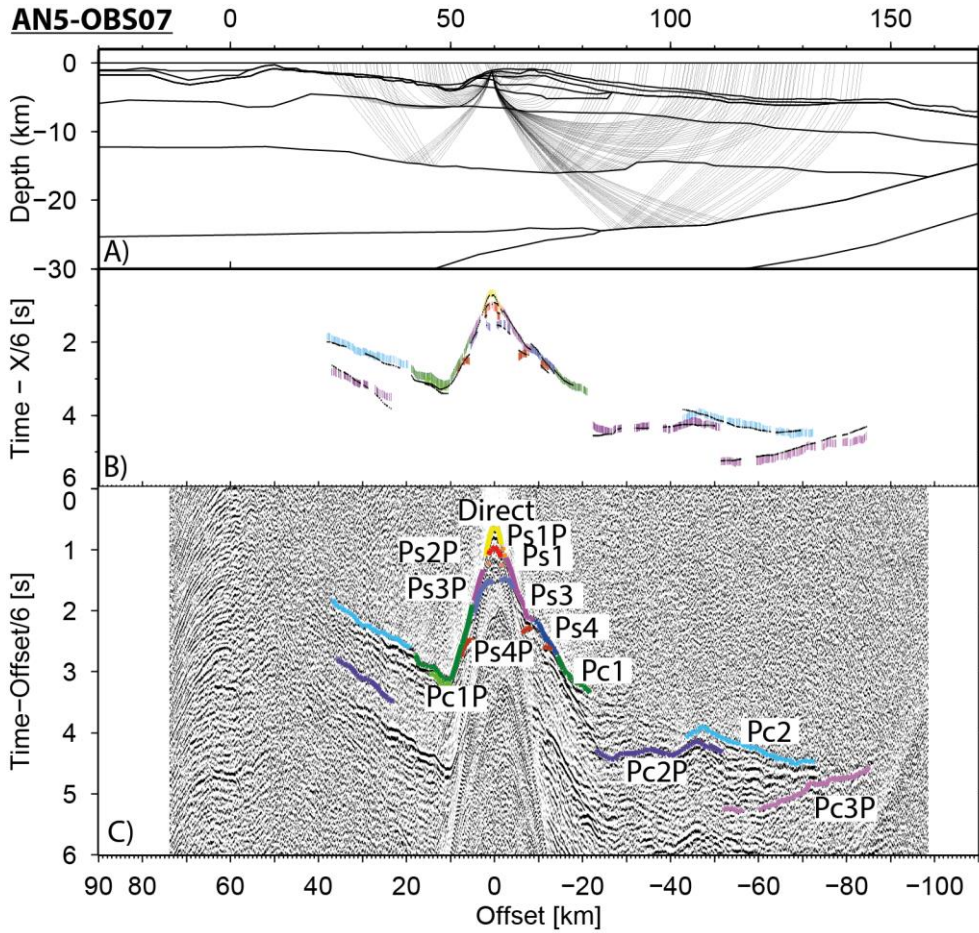


Figure 4: Modeled ray paths and wide-angle seismic sections for six different OBSs (see Figure 3 for instruments location). For each panel, (A) Ray coverage every fifth ray plotted. (B) Observed travel times (colored bars) according to phases picks and calculated travel time (solid lines). (C) OBS seismic section with picked phases. P-wave refracted phase through the  $n$ th sedimentary layer ( $PS_n$ ), the  $n$ th crust layer ( $Pc_n$ ), the Moho mantle for the upper plate ( $Pn$ ). P-wave reflected phase on the bottom of the  $n$ th sedimentary layer ( $PsnP$ ), the  $n$ th crust layer ( $PcnP$ ), on the Moho interface of the subducting plate ( $PmP$ ). P-wave reflected phase on top of the subducting plate under the mantle phase of upper plate ( $PcoP$ ).

### 207 3.3.2. Error analysis

208 Uncertainty and quality of the velocity models can be evaluated according to several parameters  
209 described in the following paragraphs.

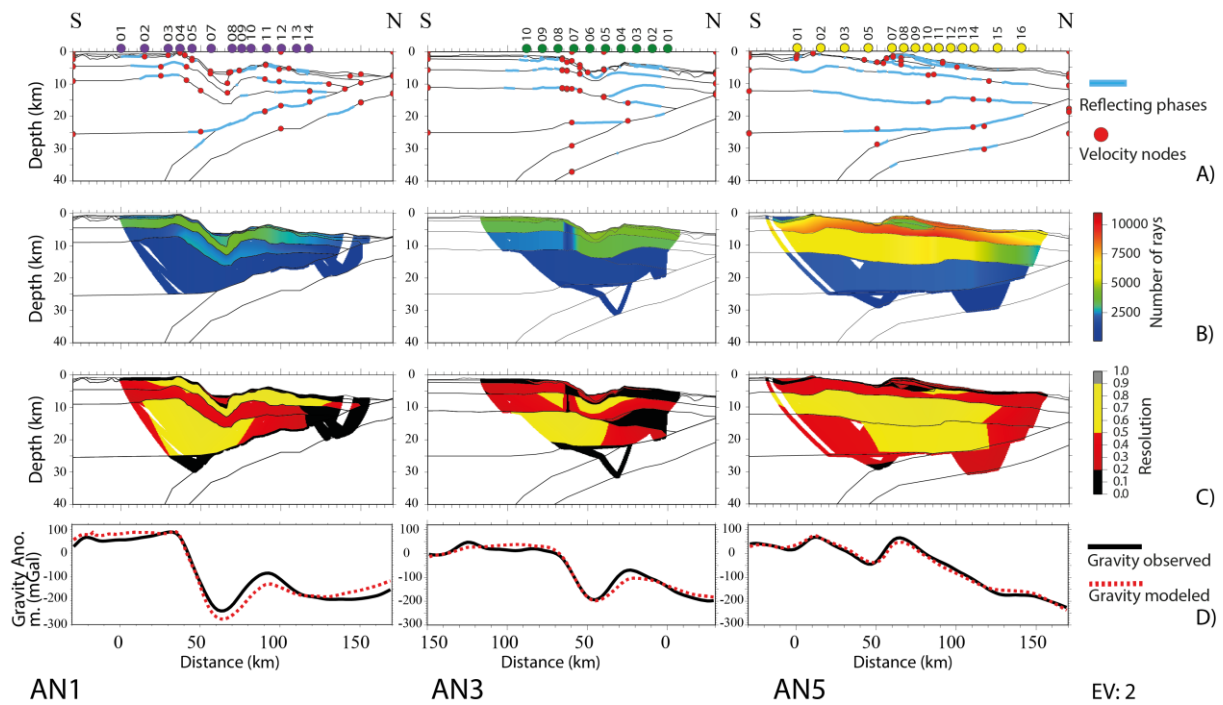
210 The root mean square (RMS) error evaluates the misfit between calculated and observed travel  
211 times. The global RMS errors are respectively 0.150 ms for model AN5, 0.158 ms for model  
212 AN1, and 0.167 ms for model AN3. RMS errors range from 0.060 ms for direct wave to 0.291  
213 ms for far-offset arrivals. On the 28787 picked arrivals on the whole OBS data set of the three  
214 presented models, 24446 picks are correctly reproduced which corresponds to 84.92% (see table  
215 in the supplementary material: misfits details for each phases).

216 The ray density shows the number of rays passing through a region of the model (Figure 5-B  
217 and in supplementary data). The ray density is twice higher along AN5 line compared to lines  
218 AN3 and AN1 due to a larger number of OBSs and a better quality of data. Nevertheless, the  
219 three models present a good ray coverage in their central and shallower parts and satisfying  
220 coverage in depth and on the sides of models.

221 The resolution factor (Figure 5-C) is calculated using the number of rays passing through a  
222 single node normalized by the number of rays passing through the layer corresponding to this  
223 node (Zelt and Smith 1992). Therefore, this factor depends on the number, the position of nodes  
224 and the lateral velocity variations in the model. Nodes with values greater than 0.5 are  
225 considered to be well resolved. Values lower than 0.5 correspond to insufficient resolution.  
226 Generally, these low resolution values correspond to the sides of velocity models. Shallow  
227 interfaces are not well constrained by turning waves from the OBS data however the geometry  
228 of these interfaces is very well constrained by MCS data, and velocities, by local reflected and  
229 refracted phases.

230 To additionally constrain our velocity models, gravity modeling was undertaken. The 2D  
231 velocity models were first converted to density models using an empirical law (Ludwig et al.  
232 1970). These density models were then used to generate a predicted free air gravity anomaly  
233 (Zelt and Smith 1992). The predicted anomalies are then compared to free-air anomalies  
234 observed and derived from satellite altimetry (Smith and Sandwell 1997) (Figure 5-D). For the  
235 three profiles, predicted and observed gravity anomalies are in very good agreement indicating  
236 a good coherency of the velocity models with the gravimetric signal.

237 To conclude, the different methods of error analysis generally indicate, that the models are well  
238 constrained for sedimentary and crustal layers and for geometry of the subducting plate except  
239 on the edges of the models. On the other hand, and probably because of a complex abrupt  
240 geometry, the structure of layers underneath the Sombrero Basin is less well constrained. Also  
241 the velocity and thickness of the subducting oceanic crust are relatively poorly constrained due  
242 to the lack of reflected and refracted phases from this layer.



243

244 *Figure 5: Resolution parameters for lines AN1, AN3 and AN5. (A) Interfaces constrain by reflecting*  
 245 *phases are highlighted in blue. Red circles correspond to the position of velocity nodes. (B) Ray density.*  
 246 *(C) Resolution parameter for velocity nodes. Grey and yellow areas are considered as well resolved (D)*  
 247 *Results from gravity modeling.*

248

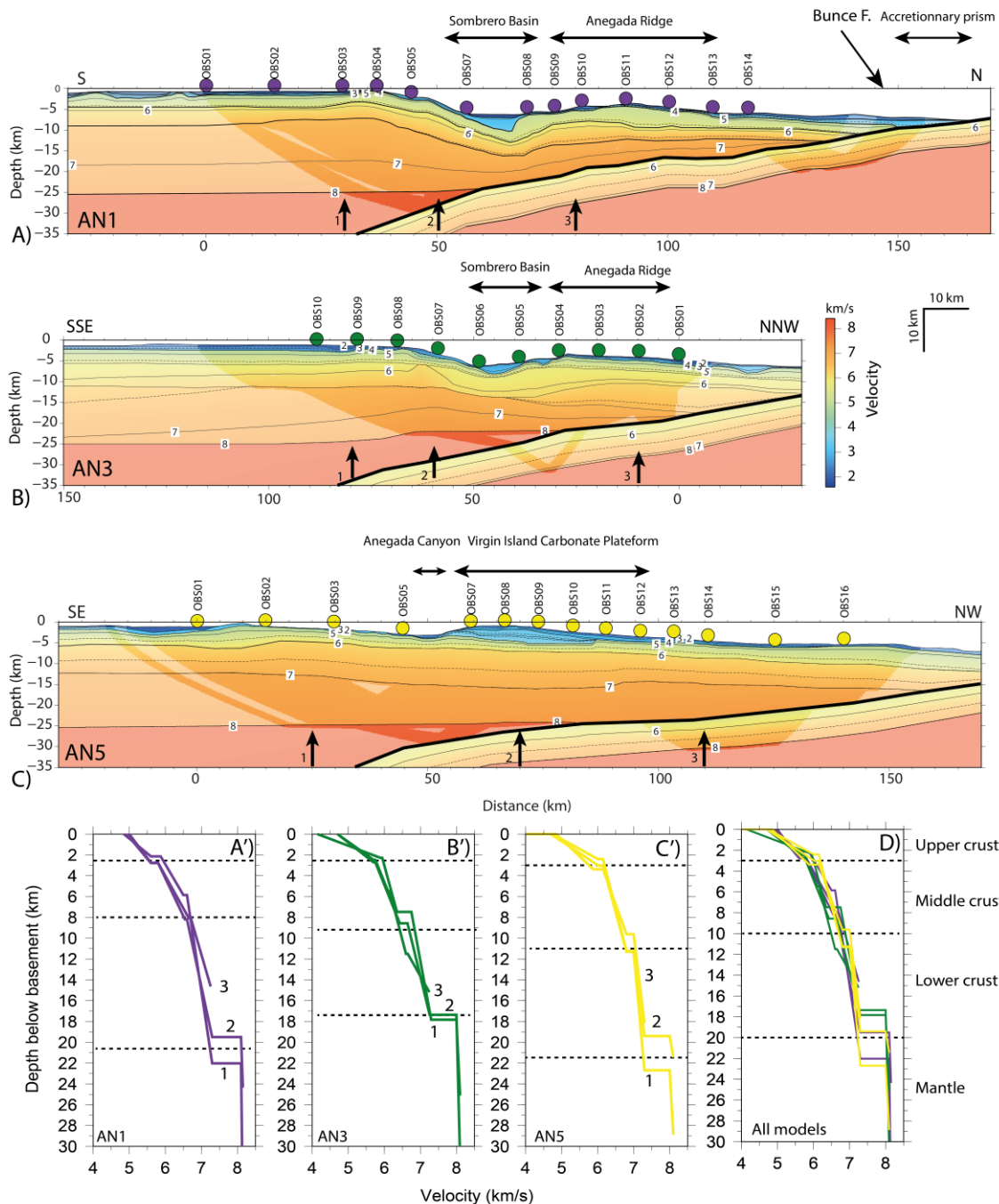


Figure 6: Final velocity models for lines AN1, AN3 and AN5 (A-B-C). Shaded areas are constrained by rays. Colored dots show location of OBSs. Velocity contours are drawn every 0.5 km/s. Thick lines depict limits of layers obtained from forward modelling and the bold one correspond to the top of the subducting plate. Vertical black arrows indicate positions of the 1D velocity depth profiles from the top of the basement for each models (A'-B'-C'). (D) Compilation of every 1D velocity depth profiles from the three models.

## 249 4. Results

250

251 The three final wide-angle velocity models (Figure 6-A-B-C) image the crust of the upper plate  
 252 corresponding to the Caribbean plate and to the north, its overlying sedimentary layers as well  
 253 as the incoming oceanic crust corresponding to the top of the subducting North American plate.

254 The incoming oceanic crust dips with an angle of approximately  $11^\circ$  for AN1 and AN3 and  $6^\circ$   
255 to  $7^\circ$  for AN5 (Figure 6-A-B-C). Few refracted and reflected rays have been modeled through  
256 and at the bottom of the layer below the accretionary prism and the forearc (Figure 6-A-B-C).  
257 It images an approximately 7-km-thick subducting plate layer with velocities ranging from 5.5  
258 to 7.1 km/s. Due to the lack of turning wave arrivals from the upper mantle, the velocities of  
259 the upper mantle of the subducting slab remain largely unresolved.

260 The models image low velocity (1.8 km/s to 3.5 km/s) layers on the top of the upper plate with  
261 an average thickness of 2 km and locally up to 5-km-thick. Between km 60 to 70 model distance  
262 for AN1 and km 50 to 60 model distance for AN3, the low velocity layer is asymmetric and  
263 reaches a thickness of 5 km. Along line AN5, the low velocity layer, located between km 55 to  
264 85 model distance, over a 30-km-wide and 5-km-thick, has a velocity of  $\sim 3.5$  km/s. Moreover,  
265 line AN1 extends to the deformation front and delineates clearly a maximum 5-km-thick unit  
266 between model distances 150 to 165 km above the subducting plate (Figure 6-A-B-C),  
267 interpreted as the accretionary prism.

268 The velocity-depth ( $V_z$ ) 1D profiles extracted beneath the sedimentary layers for models AN1,  
269 3 and 5 (Figure 6-A'-B'-C') allow to identify 3 crustal layers. For the three models, the Moho  
270 of the upper crust is approximately at 25-km-depth. The crustal thickness decreases gradually  
271 towards the deformation front from 22 km to 15 km for AN1, from 18 km to 15 km for AN3  
272 and from 23 km to 18 km for AN5. The mantle wedge appears to be located beneath the  
273 Sombrero Basin (AN1 and AN3) and beneath the Anegada Canyon (AN5). The upper crustal  
274 layer thickness ranges from 3 to 6 km with velocities from 4.70 to 6.00 km/s. The middle crustal  
275 layer thickness ranges from 5 to 9 km with velocities from 6.00 km/s to 6.80 km/s. The lower  
276 crustal layer is characterized by thicknesses from 8 to 16 km and velocities increasing from  
277 7.00 km/s to 7.30 km/s (Figure 6).

278 5. Interpretation and discussion

279 5.1. Nature and origin of the upper plate

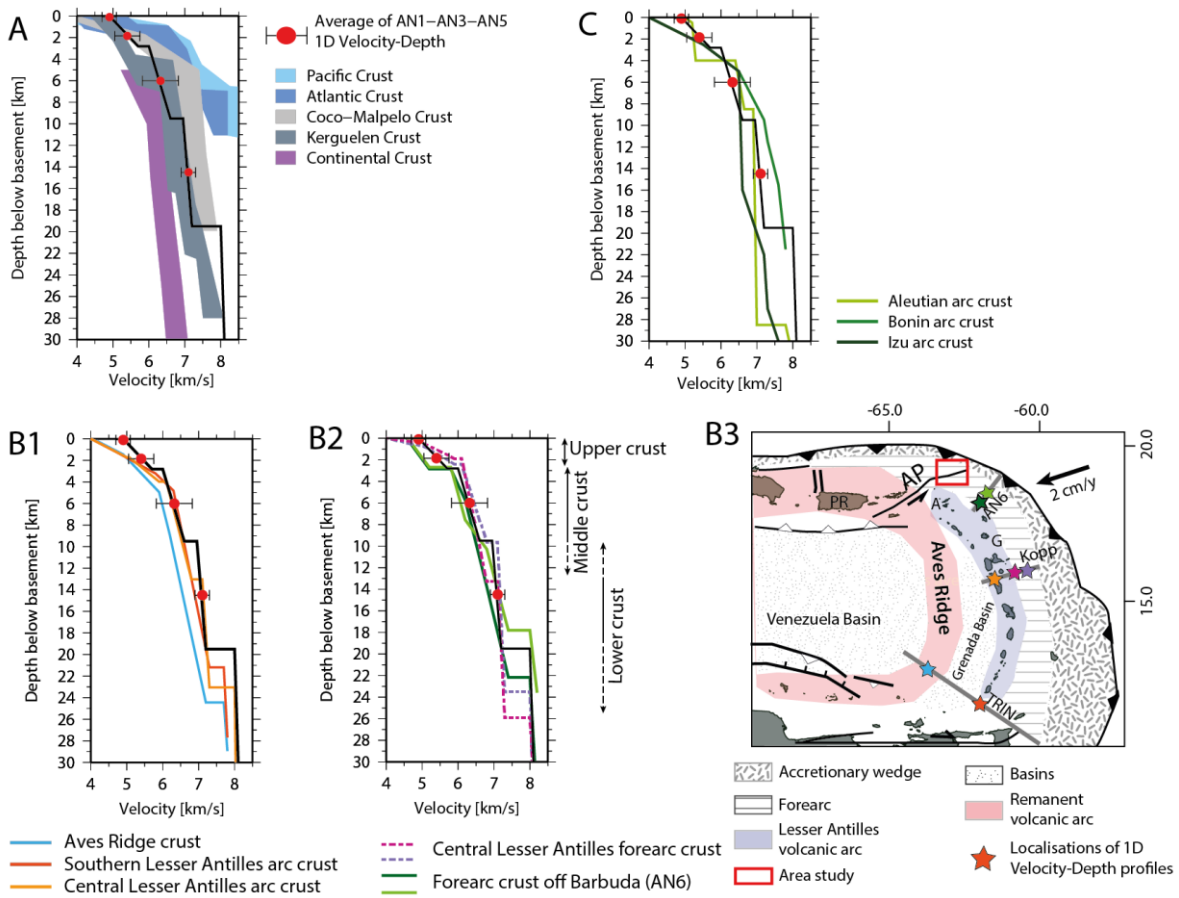


Figure 7: (A) Comparison between the average of 1D velocity depth ( $V_z$ ) profiles from models AN 1, 3 and 5 and various 1D velocity depth profiles of oceanic crust (White et al. 1992) (blue shaded area), hot spot volcanic province (grey shaded area) (Operto and Charvis 1995; Marcaillou et al. 2006) and continental crust (purple shaded area) (Christensen and Mooney 1995). Comparison with 1D velocity depth profiles of the Lesser Antilles arc crust (B1), forearc crust (B2) (Christeson et al. 2008; Kopp et al. 2011; Klingelhoefer et al. 2016).  $V_z$  profiles are localized by colored stars on the B3 map. (C) Comparison with 1D  $V_z$  profiles of Aleutian, Bonin and Izu arc crusts (Shillington et al. 2004; Kodaira et al. 2010).

280

281 5.1.1. Sedimentary layers

282 Along every profile, layers with velocities ranging from 2 to 3.5 km/s are likely to be of  
 283 sedimentary origin. Three domains with such velocities are reported. The frontal part in line  
 284 AN1 consists in a 15-km-thick accretionary prism limited southward by the Bunce Fault where  
 285 the velocity suddenly rises up. This fault thus also corresponds with the backstop, which  
 286 separates the accretionary prism from the forearc basement. In models AN1 and AN3, the  
 287 asymmetric Sombrero Basin contains a thick sedimentary filling (Laurencin et al. 2017). In  
 288 model AN5, a high-velocity (3.5 km/s) 3-km-thick layer corresponds with the northeastern part  
 289 of Virgin Islands carbonate platform, which is consistent with limestone dredge 120D from  
 290 cruise Arcante3 (Bouysse et al. 1985) located at km 50-distance in model AN5.

291                   5.1.2. Nature of the crust

292   Beneath the sedimentary layers, models show three crustal layers with velocities ranging from  
293   4.7 km/s to 7.1 km/s. In the upper crust, the velocity (4.7 to 6.0 km/s) is similar to the Izu-Bonin  
294   margin (Figure 7-C) and ~0.5 km/s higher than at the Central and Southern Lesser Antilles  
295   (Figure 7-B1). Thus it is consistent with a volcanoclastic, intrusive and extrusive rocks  
296   uppermost layer (Christeson et al. 2008; Kodaira et al. 2010; Kopp et al. 2011). The velocity  
297   variations probably depend on the fluid content, fracturing, porosity and alteration state of  
298   rocks. The velocities and thicknesses of the middle and lower layers are closely consistent with  
299   velocity models in the Central (Kopp et al. 2011) and Southern (Christeson et al. 2008) Lesser  
300   Antilles arc (Figure 7-B1) and for the interpreted arc-intermediate crustal layers at Aleutian and  
301   Izu-Bonin subduction zones (Figure 7-C), (Shillington et al. 2004; Kodaira et al. 2010). It  
302   supports the interpreted felsic to intermediate and gabbroic nature for the middle and lower  
303   layers respectively.

304                   5.1.3. Origin of crust

305   The wide-angle-derived structure for the Northern Lesser Antilles margin shows strong  
306   similarities in velocities and thicknesses with the Kerguelen, Cocos-Malpelo, Aleutian and Izu-  
307   Bonin margins (Figure 7). However, for these margins the oceanic crust is interpreted as  
308   thickened mainly by subduction magmatism for the Aleutian and Izu-Bonin margin (Shillington  
309   et al. 2004; Kodaira et al. 2010) and by hotspot magmatism for the Kerguelen and Cocos-  
310   Malpelo provinces.

311   Previous velocity studies in the Central and Southern Lesser Antilles (Christeson et al. 2008;  
312   Kopp et al. 2011) and petrological studies of Hispaniola rocks samples and Caribbean plateau  
313   drilling samples (Kerr et al. 2003) suggest an oceanic basement thickened by hotspot  
314   magmatism. The similar velocity and thickness structures in the Northern Lesser Antilles and  
315   in Kerguelen and Cocos-Malpelo provinces (Figure 7-A), Southern and Central Lesser Antilles  
316   arc (Figure 7-B1) are consistent with this origin.

317   The dredged rocks, dated from Cretaceous to Paleocene, in the study area (Bouysse et al. 1985)  
318   suggest that the basement in the Northern Lesser Antilles is likely affected by the Cretaceous  
319   to Eocene '*Great Arc of the Caribbean*' volcanism. This suggests a basement thickening by  
320   subduction volcanism in the Northern Lesser Antilles.

321   At the Aleutian and Izu-Bonin subduction zones, the thickening by subduction volcanism shows  
322   velocities > 7.3 km/s at the base of the margin basement. This high-velocity layer is missing in  
323   the Northern Lesser Antilles models (Figure 7-C). Moreover, during the Eocene (Figure 1-D),  
324   the '*Great Arc of the Caribbean*' volcanism likely migrated eastward to the Lesser Antilles arc.  
325   The Lesser Antilles volcanism has a very low magma production rates and does not mainly  
326   thickened the Lesser Antilles crust (e.g. Christeson et al. 2008), The subduction volcanism has  
327   possibly not contributed significantly to the margin basement thickening during the activity of  
328   the '*Great Arc of the Caribbean*' either.

329   Thus, the Northern Lesser Antilles margin is consistent with an oceanic affinity crust mainly  
330   thickening by hotspot magmatism and to a lesser extent by the '*Great Arc of the Caribbean*'  
331   volcanism.

332 5.2. Subducting plate bulge, causes and consequences

333 5.2.1. Geometry of the slab

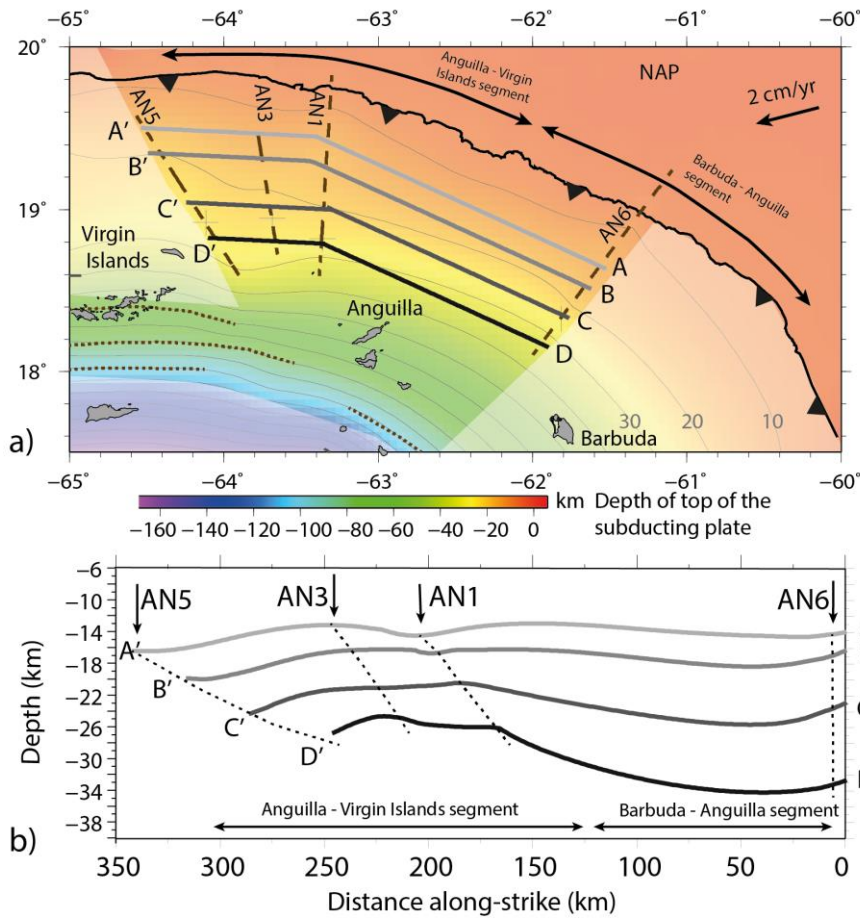


Figure 8: Depth of the top of the subducting plate (a) in 3D (b) along 2D along-strike sections AA', BB', CC', and DD' located at 35, 50, 75, 105 km from the trench respectively. Black dotted lines AN1, AN3, AN5 (this study) and AN6 (Klingelhoefer et al. 2016) show the location for wide angle lines. Brown dotted lines are isohypocenter depths of earthquakes from McCann and Sykes (1984). NAP: North American Plate.

334

335 We use various datasets to determine the geometry of the subducting plate: (1) the location and  
 336 depth of the top of the slab where it is constrained by reflected rays of the velocity models along  
 337 lines AN1-3-5 (this study) and AN6 (Klingelhoefer et al. 2016), (2) the subduction earthquakes  
 338 (McCann and Sykes 1984) under the volcanic islands (small dotted brown segments), and (3)  
 339 the bathymetry of the trench and the plunging plate before subduction. Where unconstrained,  
 340 the depth of the top of the slab is interpolated (Figure 8-a). This interpolation is unconstrained  
 341 in areas located to the west of line AN5 and to the south-east of line AN6 that are beyond the  
 342 scope of this study.

343 2D profiles parallel to the deformation front, AA', BB', CC' and DD' show the along-strike  
 344 variations in depth to the top of the slab at 35, 50, 75 and 105 km distance from the trench  
 345 respectively (Figure 8-b). The slab depth at 35 and 50 km from the trench does not significantly  
 346 vary along-strike (AA' and BB' in Figure 8 a-b). In contrast, at 75 km from the trench, the slab  
 347 is 26-km-deep offshore of the Barbuda-Anguilla margin segment and 20-km-deep offshore of

348 the Anguilla-Virgin Islands margin segment (CC' in Figure 8-a-b). Moreover, at 105 km, the  
349 slab depth varies from 36 km to 26 km between this two segments (DD' in Figure 8-a-b).

350 Thus, at shallow to intermediate depths (20 to 35 km), beyond 75 km from the deformation  
351 front, the slab is 25% shallower beneath the Anguilla-Virgin Islands margin segment, than  
352 beneath the Barbuda Anguilla segment. Moreover, a tear fault in the slab between Puerto Rico  
353 and Virgin Islands possibly accommodates the shallow slab subduction under a curved margin  
354 by decreasing the slab dip to the east in the Northern Lesser Antilles (Ten Brink 2005; Meighan  
355 et al. 2013). This eastward shallowing of the slab beneath the Virgin Islands margin segment is  
356 strongly consistent with our results. The distance between models AN6 and AN1 does not allow  
357 us to constrain the precise shape of the slab related to the change in dip angle. Somewhere  
358 beneath Barbuda and Virgin Islands, a progressive large-scale flexure, a localized shear zone  
359 or a tear fault possibly accounts for this slab dip change. Either ways, this slab dip change, to  
360 the northeast of Barbuda and the Puerto Rico tear fault may allow a certain buoyancy degree  
361 for the slab that is shallower beneath the Anguilla-Virgin Islands margin segment.

### 362 5.2.2. Origin of slab geometry variations

363 In the following, we discuss several causes of variations in slab geometry and in  
364 particular in slab dips. Hikurangi, Japan and Northern Luzon subduction zones for example,  
365 also show complex slab geometries (Barker et al. 2009; Bautista et al. 2016). These authors  
366 conclude that chemical reactions, fluid release within the subducting plates as well as  
367 subduction of topographic highs mainly control the slab geometry. Seismic, heat flow and  
368 bathymetric data collected along the incoming North American plate show evidences for a large  
369 subducting basement patch of magmatic-poor mantellic-dominated rocks (Marcaillou et al.  
370 2017). This dense and poorly resistant basement patch, subducting beneath the Antigua-  
371 Anguilla margin segment, possibly decreases the slab buoyancy.

372 Subducting buoyant ridges or seamounts may also result locally in a shallower slab as  
373 shown at numerous margins (e.g. Bautista et al. 2016) or reproduced in analogue models (e.g.  
374 Martinod et al. 2013). Seismic and bathymetric data highlight the extent of the Barracuda Ridge  
375 beneath the margin offshore of Antigua and Barbuda (Laigle et al. 2013). However, the Main  
376 Ridge (Figure 2) is a small-scale, thin and uncompensated topographic feature restricted to the  
377 Virgin Islands outer slope (Grindlay et al. 2005). The possible continuity between these ridges  
378 beneath the margin, as proposed by Mccann and Sykes (1984) is unclear. In any case, the  
379 subduction of a possibly buoyant ridge beneath the Antigua margin segment, where the slab is  
380 steep, or beneath the whole study area do not provide a convincing explanation for the  
381 northward shallowing of the slab.

382 North of the Caribbean, the 300 000-km<sup>2</sup>-area Bahamas Bank is a carbonate platform  
383 located on the North Atlantic plate and in collision at the Hispaniola trench. This collision  
384 possibly modifies the slab buoyancy offshore Hispaniola (e.g. Laó-dávila 2014) but is unlikely  
385 to interfere with the subduction system beneath the Anguilla-Virgin Islands margin.

386 The curved shape of the margin may imply geometrical complexities and discontinuities  
387 in the slab subduction. Larged scale, 3D numerical model of oblique subduction have shown  
388 slab folding that generates along-strike variations in slab dip and in upper plate topography  
389 (Cerpa et al. 2015). Moreover, modelling slab subduction beneath convex margins results in  
390 focussing the compressive strain in the upper plate toward the convexity axis generating margin  
391 uplift where the convexity climaxes (Bonnardot et al. 2008). These models highlight the  
392 influence of the plate boundary geometry and the subduction obliquity onto the slab dip angle  
393 and the deformation of the upper plate, that are strongly consistent with our results. At 18.5°N-

394 60.5°W, to the northeast of Antigua-Barbuda, a kink in the subduction line shapes a convex  
395 plate boundary and results in a rapid increase of the subduction obliquity (Figure 2). To the  
396 north, the margin is spiked with numerous uplifted carbonate platform and the slab shallows  
397 consistently with the expected slab folding due to subduction obliquity (Cerpa et al. 2015) and  
398 the compressive strain focussing toward the convexity axis (Bonnardot et al. 2008). These  
399 consistencies suggest that the shallower slab beneath the Anguilla-Virgin Islands margin  
400 segment observed in wide-angle data is related to the margin convexity and the subduction  
401 obliquity.

### 402 5.2.3. Tectonic partitioning and interplate coupling

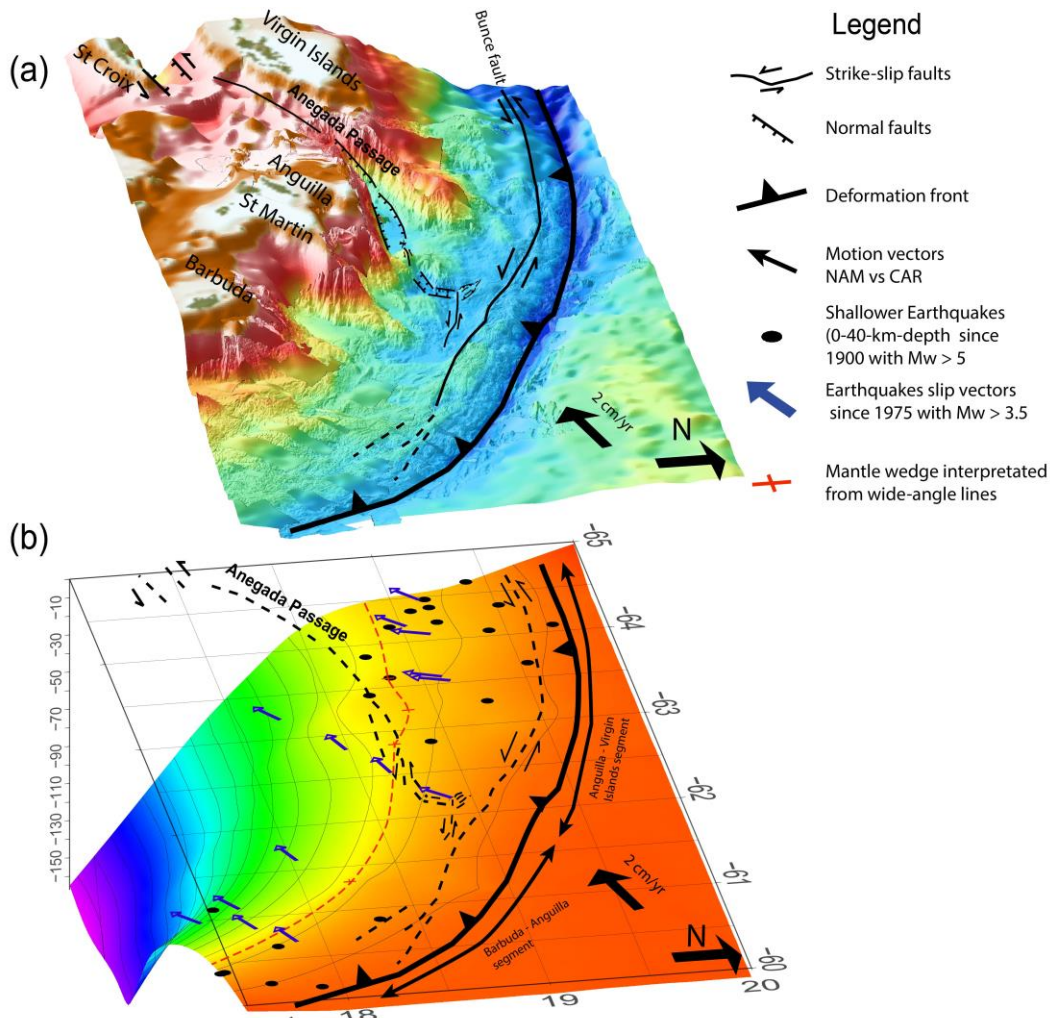
403 Varying geometry of subduction interface possibly controls variations in interplate  
404 seismic coupling, seismogenesis and margin tectonic deformation, in subduction zones as  
405 proposed in Hikurangi (e.g. Barker et al. 2009), North Chile (e.g. Boutelier and Oncken 2010)  
406 and Japan (e.g. Ito et al. 2009).

407 On a large scale, geodetic data suggest that the Lesser Antilles margin is only partially  
408 coupled between Barbuda and Virgin Islands (Manaker et al. 2008; Symithe et al. 2015).  
409 However, in subduction zones, structural heterogeneities possibly generate local variations in  
410 subduction interface properties and interplate seismic coupling that can be documented with  
411 dense local GPS deployments (e.g. Marcaillou et al. 2016). Thus, the slab shallowing may  
412 locally increase the interplate seismic coupling beneath the Anguilla-Virgin Islands segment.  
413 For the Northern Lesser Antilles no mega-thrust earthquake cycle has been detected yet. Thus,  
414 despite local variation in seismic coupling, the accumulation of stress at the subduction interface  
415 increases very slowly and/or a large part is relaxed by the deformations observed on the upper  
416 plate margin as proposed by Manaker et al. (2008) and Symithe et al. (2015).

417 In Northern Lesser Antilles, the earthquakes with thrust focal mechanism ( $M_w > 3.5$   
418 from CMT catalog, since 1976) and shallow, 0-40-km-depth, earthquakes (PDE/NEIC catalog,  
419  $M_w > 5$ , since 1900) are more numerous beneath the Anguilla-Virgin Islands margin segment  
420 than beneath the Barbuda-Anguilla margin segment (Figure 9-b). Mccann and Sykes (1984)  
421 propose that this seismic heterogeneity is controlled by local tectonic complexity related to  
422 subducting reliefs as the Main Ridge (Figure 2). This northwestward increase in seismicity  
423 raises the question of a possible relation with the slab northward shallowing. Moreover, at  
424 shallow depths (18-30 km), the slab shallowing may increase the length of the brittle interface  
425 between the upper and the downgoing crusts. This may increase the length of the seismogenic  
426 zone and the subduction seismic activity.

427 The major EW-trending strike-slip Anegada Passage accommodates at least a part of the  
428 tectonic partitioning due to the plate convergence obliquity (Laurencin et al. 2017). It is  
429 noteworthy that the Anegada Passage entails the margin above the area where the slab dip  
430 decreases (Figure 9-a-b) which raises the question of a possible relation between the slab  
431 northward shallowing and the onset of this partitioning. 3D models of convex subduction zones  
432 point out that curved margin zones focus compressive strain and uplifts and are thus preferential  
433 zones for strike-slip faults initiation (Bonnardot et al. 2008). Thus, we propose that the slab  
434 shallowing under Anguilla-Virgin Islands segment increases locally the transfer of interplate  
435 shear stresses to the overriding plate and also favors partitioning deformation.

436



437

438 *Figure 9: (a) 3D view of the Northern Lesser Antilles bathymetry and the interpreted tectonic*  
 439 *deformation pattern within the upper plate (Laurencin et al. 2017) (b) Top of the subducting plate with*  
 440 *projection of some margin tectonic deformations features (dotted black lines), shallower earthquakes*  
 441 *(0-40-km-depth) since 1900 with Mw > 5 (black circles), subducting earthquakes slip vectors since 1976*  
 442 *from CMT global catalog (Mw > 3.5), (blue arrows) and the localization of the mantle wedge (dotted*  
 443 *red line)*

## 444 6. Conclusions

445 Wide-angle models across the Northern Lesser Antilles forearc provide new insights into the  
 446 geometry of the subducting North America plate, the nature and origin of the northeastern upper  
 447 caribbean margin and the consequences for tectonic deformations and seismogenesis:

448 1) The velocity and thickness structure across the Northern Lesser Antilles margin is consistent  
 449 with an oceanic affinity crust over-thickened by hotspot magmatism and to a lesser extent by  
 450 the subduction volcanism of the ‘Great Arc of the Caribbean’.

451 2) The depth to the top of the subducting plate is 25% shallower under the Anguilla-Virgin  
 452 Islands segment than under the Barbuda-Anguilla segment. This slab shallowing is possibly  
 453 related to the effects of the increasing subduction obliquity of the North America Plate beneath  
 454 the convex Northern Lesser Antilles margin.

455 3) We propose that the shallower slab under the Anguilla-Virgin Islands segment locally  
456 increases the interplate shear stress favoring the tectonic partitioning observed in the Anegada  
457 Passage. This slab shallowing may also locally increase the interplate coupling, even though it  
458 is low on a large scale, which is consistent with the northward increasing number of  
459 earthquakes.

#### 460 **Acknowledgments**

461 We thanks the Captain and the crew of the RVs *L'Atalante* and *Pourquoi Pas?* We are indebted  
462 to the Genavir Technicians for bathymetry processing, the successful completion of the seismic  
463 acquisition and to the scientific crew for the pre-processing undertaken onboard. We  
464 acknowledge financial support from Region Bretagne for PhD fellowship of M. Laurencin. We  
465 thank Labex MER, INSU and Antilles University of Guadeloupe Island for the partly financing  
466 cruises. Most of the figures were drafted using GMT and Qgis software. All data of the  
467 ANTITHESIS cruises are available on demand at SISMER ([www.ifremer.fr/sismer/](http://www.ifremer.fr/sismer/)).

468

469 **References**

470 Auffret, Y., Pelleau, P., Klingelhoefer, F., Géli, L., Crozon, J., Lin, J., and Sibuet, J-C. 2004. MicroOBS : a new  
471 generation of ocean bottom seismometer. *First Break* 22: 41–47.

472 Barker, D. H. N., Sutherland, R., Henrys, S., and Bannister, S. 2009. Geometry of the Hikurangi subduction thrust  
473 and upper plate, North Island, New Zealand. *Geochemistry, Geophysics, Geosystems* 10: 1–23.  
474 doi:10.1029/2008GC002153.

475 Bautista, B. C., Bautista, M. L. P., Oike, K., Wu, F. T., and Punongbayan, R. S. 2016. A new insight on the  
476 geometry of subducting slabs in Northern Luzon , Philippines in northern Luzon , Philippines. *Tectonics*  
477 339: 279–310. doi:10.1016/S0040-1951(01)00120-2.

478 Van Benthem, S., Govers, R., Spakman, W., and Wortel, R. 2013. Tectonic evolution and mantle structure of the  
479 Caribbean. *Journal of Geophysical Research: Solid Earth* 118: 3019–3036. doi:10.1002/jgrb.50235.

480 Bernard, P., and Lambert, J. 1988. Subduction and seismic hazard in the Northern Lesser Antilles : Revision of  
481 the historical seismicity. *Bulletin of the Seismological Society of America* 78: 1965–1983.

482 Bonnardot, M., Hassani, R., Tric, E., and Ruellan, E. 2008. Effect of margin curvature on plate deformation in a  
483 3-D numerical model of subduction zones. *Geophysical Journal International* 173: 1084–1094.  
484 doi:10.1111/j.1365-246X.2008.03752.x.

485 Boschman, L. M., Van Hinsbergen, D. J. J., Torsvik, T. H., Spakman, W., and Pindell, J. L. 2014. Earth-Science  
486 Reviews Kinematic reconstruction of the Caribbean region since the Early Jurassic. *Earth Science Reviews*  
487 138. Elsevier B.V.: 102–136. doi:10.1016/j.earscirev.2014.08.007.

488 Boutelier, D. A., and Oncken, O. 2010. Role of the plate margin curvature in the plateau buildup : Consequences  
489 for the central Andes. *Journal of Geophysical Research* 115: 1–17. doi:10.1029/2009JB006296.

490 Bouysse, P., Andreieff, P., Richard, M., Baubron, J. C., Mascle, A., Maury, R. C., and Westercamp, D. 1985. Aves  
491 Swell and northern Lesser Antilles Ridge: rock-dredging results from ARCANTE 3 cruise. In *Géodynamique*  
492 *des caraïbes. Symposium*, 65–76.

493 Bouysse, P., and Westercamp, D. 1990. Subduction of Atlantic aseismic ridges and Late Cenozoic evolution of  
494 the Lesser Antilles island arc. *Tectonophysics*. doi:10.1016/0040-1951(90)90180-G.

495 Ten Brink, U. 2005. Vertical motions of the Puerto Rico Trench and Puerto Rico and their cause. *Journal of*  
496 *Geophysical Research* 110: 1–16. doi:10.1029/2004JB003459.

497 Ten Brink, U., Danforth, W., Polloni, C., Andrews, B., Llanes, P., Smith, S., Parker, E., and Uozumi, T. 2004.  
498 New seafloor map of the Puerto Rico trench helps assess earthquake and tsunami hazards. *Eos, Transactions*  
499 *American Geophysical Union* 85: 349–360. doi:10.1029/2004EO370001.

500 Cerpa, N.G., Araya, R., Gerbault, M., and Hassani, R. 2015. Relationship between slab dip and topography  
501 segmentation in an oblique subduction zone : Insights from numerical modeling. *Geophysical Research*  
502 *Letters* 42: 1–10. doi:10.1002/2015GL064047.

503 Christensen, N. I., and Mooney, W. D. 1995. Seismic velocity structure and composition of the continental crust:  
504 A global view. *Journal of Geophysical Research* 100: 9761–9788. doi:10.1029/95JB00259.

505 Christeson, G. L., Mann, P., Escalona, A., and Aitken, T. J. 2008. Crustal structure of the Caribbean - Northeastern  
506 South America arc-continent collision zone. *Journal of Geophysical Research* 113: 1–19.  
507 doi:10.1029/2007JB005373.

508 DeMets, C., Jansma, P., Mattioli, G., Dixon, T. H., Farina, F., Bilham, R., Calais, E., and Mann, P. 2000. GPS  
509 geodetic constraints on Caribbean-North America plate motion. *Geophysical Research Letters* 27: 437–440.

510 Feuillet, N., Beauducel, F., and Tapponnier, P. 2011. Tectonic context of moderate to large historical earthquakes  
511 in the Lesser Antilles and mechanical coupling with volcanoes. *Journal of Geophysical Research* 116: 1–  
512 26. doi:10.1029/2011JB008443.

513 Fitch, T J. 1972. Plate Convergence, Transcurrent Faults, and Internal Deformation Adjacent to Southeast Asia  
514 and the Western Pacific. *Journal of Geophysical Research* 77: 4432–4460.

515 Grindlay, N. R., Mann, P., Dolan, J. F., and Van Gestel, J. P. 2005. Neotectonics and subsidence of the northern  
516 Puerto Rico-Virgin Islands margin in response to the oblique subduction of high-standing ridges. Edited by  
517 Paul Mann. *Geological Society of America Special Papers* 385: 31–60.

518 Hayes, G. P., Wald, D. J., and Johnson, R. L. 2012. Slab1.0 : A three-dimensional model of global subduction  
519 zone geometries. *Journal of Geophysical Research* 117: 1–15. doi:10.1029/2011JB008524.

520 Ito, Tanio., Kojima, Yuji., Kodaira, Shuichi., Sato, Hiroshi., Kaneda, Yoshiyuki., Iwasaki, Takaya., Kurashimo,  
521 Eiji., Tsumura, Noriko., Fujiwara, Akira., Miyauchi, Takahiro., Hirata, Naoshi., Harder, Steven., Sato,  
522 Takeshi., and Ikawa, Takeshi. 2009. Tectonophysics Crustal structure of southwest Japan , revealed by the  
523 integrated seismic experiment Southwest Japan 2002. *Tectonophysics* 472. Elsevier B.V.: 124–134.  
524 doi:10.1016/j.tecto.2008.05.013.

- 525 James, K. H. 2009. In situ origin of the Caribbean: discussion of data. *Geological Society, London, Special*  
526 *Publications* 328: 77–125. doi:10.1144/SP328.3.
- 527 Jany, I., Scanlon, K. M., and Mauffret, A. 1990. Geological interpretation of combined Seabeam, Gloria and  
528 seismic data from Anegada Passage (Virgin Islands, north Caribbean). *Marine Geophysical Researches* 12:  
529 173–196. doi:10.1007/BF02266712.
- 530 Jolly, Wayne T., Lidiak, Edward G., and Dickin, Alan P. 2008. Bimodal volcanism in northeast Puerto Rico and  
531 the Virgin Islands ( Greater Antilles Island Arc ): Genetic links with Cretaceous subduction of the mid-  
532 Atlantic ridge Caribbean spur. doi:10.1016/j.lithos.2007.10.008.
- 533 Kerr, A.C., White, R.V., Thompson, P. M. E., and Saunders, A.D. 2003. No oceanic plateau-no Caribbean plate?  
534 The seminal role of an oceanic plateau in Caribbean plate evolution. In *The Circum-Gulf of Mexico and the*  
535 *Caribbean: Hydrocarbon habitats, basin formation, and plate tectonics: AAPG Memoir* 79, C. Bartoli, 126–  
536 168.
- 537 Klingelhoefer, F., Laurencin, M., Marcaillou, B., Benabdellouahed, M., Graindorge, D., Maury, T., Biari, Y.,  
538 Evain, M., Chang, E., Scalabrin, C., and Lebrun, J.-F. 2016. Relations between the deep crustal structure  
539 and fluid escape structures at the Lesser Antilles Island arc. *Poster AGU*.
- 540 Kodaira, S., Noguchi, N., Takahashi, N., Ishizuka, O., and Kaneda, Y. 2010. Evolution from fore-arc oceanic crust  
541 to island arc crust: A seismic study along the Izu-Bonin fore arc. *Journal of Geophysical Research*  
542 115Kodaira: 1–20. doi:10.1029/2009JB006968.
- 543 Kopp, H., Weinzierl, W., Becel, A., Charvis, P., Evain, M., Flueh, E. R., Gailler, A., Galve, A., Hirn, A.,  
544 Kandilarov, A., Klaeschen, D., Laigle, M., Papenberg, C., Planert, L., and Roux, E. 2011. Deep structure of  
545 the central Lesser Antilles Island Arc: Relevance for the formation of continental crust. *Earth and Planetary*  
546 *Science Letters* 304. Elsevier B.V.: 121–134. doi:10.1016/j.epsl.2011.01.024.
- 547 Laigle, M., Becel, A., de Voogd, B., Sachpazi, M., Bayrakci, G., Lebrun, J.-F., Evain, M., and Group, the “Thales  
548 was Right” Seismic Reflection working. 2013. Along-arc segmentation and interaction of subducting ridges  
549 with the Lesser Antilles Subduction forearc crust revealed by MCS imaging. *Tectonophysics* 603: 32–54.  
550 doi:10.1016/j.tecto.2013.05.028.
- 551 Laó-dávila, D. 2014. Collisional zones in Puerto Rico and the northern Caribbean. *Journal of South American*  
552 *Earth Sciences* 54. Elsevier Ltd: 1–19. doi:10.1016/j.jsames.2014.04.009.
- 553 Laurencin, M., Marcaillou, B., Graindorge, D., Klingelhoefer, F., Lallemand, S., Laigle, M., and Lebrun, J.F. 2017.  
554 The polyphased tectonic evolution of the Anegada Passage in the northern Lesser Antilles subduction zone.  
555 *Tectonics* 36: 17. doi:10.1002/2017TC004511.
- 556 López, A. M., Stein, S., Dixon, T., Sella, G., Calais, E., Jansma, P., Weber, J., and LaFemina, P. 2006. Is there a  
557 northern Lesser Antilles forearc block? *Geophysical Research Letters* 33: 2–5. doi:10.1029/2005GL025293.
- 558 Ludwig, W. J., Nafe, J. E., and Drake, C. L. 1970. Seismic refraction. *The sea* 4: 53–84.
- 559 Manaker, D. M., Calais, E., Freed, A. M., Ali, S. T., Przybylski, P., Mattioli, G., Jansma, P., Prépetit, C., and De  
560 Chabaliér, J. B. 2008. Interseismic plate coupling and strain partitioning in the Northeastern Caribbean.  
561 *Geophysical Journal International* 174: 889–903. doi:10.1111/j.1365-246X.2008.03819.x.
- 562 Mann, P., Grindlay, N. R., and Abrams, L. J. 2005. Neotectonics of southern Puerto Rico and its offshore margin.  
563 *Geological Society of America Special Papers* 385: 173–214. doi:10.1130/0-8137-2385-X.173.
- 564 Marcaillou, B., Charvis, P., and Collot, J.-Y. 2006. Structure of the Malpelo Ridge (Colombia) from seismic and  
565 gravity modelling. *Marine Geophysical Researches* 27: 289–300. doi:10.1007/s11001-006-9009-y.
- 566 Marcaillou, B., Collot, J.-Y., Ribodetti, A., Mahamat, A.-A., and Alvarado, A. 2016. Seamount subduction at the  
567 North-Ecuadorian convergent margin: Effects on structures, inter-seismic coupling and seismogenesis.  
568 *Earth and Planetary Science Letters* 433. Elsevier B.V.: 146–158. doi:10.1016/j.epsl.2015.10.043.
- 569 Marcaillou, B., and Klingelhoefer, F. 2013. ANTITHESIS-1-Leg1 Cruise, RV L’Atalante. *Cruises Report*.  
570 doi:10.17600/13010070.
- 571 Marcaillou, B., Klingelhoefer, F., Laurencin, M., Biari, Y., Graindorge, D., Lebrun, J.-F., Laigle, M., and  
572 Lallemand, S.E. 2017. The Subduction of an Exhumed and Serpentinized Magma-Poor Basement Beneath  
573 the Northern Lesser Antilles Reveals the Early Tectonic Fabric at Slow-Spreading Mid-Oceanic Ridges. In  
574 *T31D-0656*. AGU Fall Meeting. New Orleans.
- 575 Martinod, J., Guillaume, B., Espurt, N., Faccenna, C., Funiciello, F., and Regard, V. 2013. Tectonophysics Effect  
576 of aseismic ridge subduction on slab geometry and overriding plate deformation: Insights from analogue  
577 modeling. *Tectonophysics* 588. Elsevier B.V.: 39–55. doi:10.1016/j.tecto.2012.12.010.
- 578 McCaffrey, R. 1992. Oblique plate convergence, slip vectors, and forearc deformation. *Journal of Geophysical*  
579 *Research*. doi:10.1029/92JB00483.
- 580 McCann, W. R., Nishenko, S. P., Sykes, L. R., and Krause, J. 1979. Seismic gaps and plate tectonics: Seismic  
581 potential for major boundaries. *Pure and Applied Geophysics PAGEOPH* 117: 1082–1147.

582           doi:10.1007/BF00876211.

583 McCann, W. R., and Sykes, L. R. 1984. Subduction of Aseismic Ridges beneath the Caribbean Plate : implications  
584           for the tectonics and seismic potential of the northeastern caribbean. *Journal of Geophysical Research* 89:  
585           4493–4519.

586 Meighan, H. E., Pulliam, J., Ten Brink, U., and López-Venegas, A. M. 2013. Seismic evidence for a slab tear at  
587           the Puerto Rico Trench. *Journal of Geophysical Research: Solid Earth* 118: 2915–2923.  
588           doi:10.1002/jgrb.50227.

589 Meschede, M., and Frisch, W. 1998. A plate-tectonic model for the Mesozoic and Early Cenozoic history of the  
590           Caribbean plate. *Tectonophysics* 296: 269–291. doi:10.1016/S0040-1951(98)00157-7.

591 Neill, I., Kerr, A. C., Hastie, A. R., Stanek, K.-P., and Millar, I. L. 2011. Origin of the Aves Ridge and Dutch-  
592           Venezuelan Antilles: interaction of the Cretaceous “Great Arc” and Caribbean-Colombian Oceanic Plateau?  
593           *Journal of Geological Society, London* 168: 333–347. doi:10.1144/0016-76492010-067.

594 Operto, S., and Charvis, P. 1995. Kerguelen Plateau: a volcanic passive margin fragment? *Geology* 23: 137–140.  
595           doi:10.1130/0091-7613.

596 Pindell, J. L., and Kennan, L. 2009. Tectonic evolution of the Gulf of Mexico, Caribbean and northern South  
597           America in the mantle reference frame: an update. *Geological Society, London, Special Publications* 328:  
598           1–55. doi:10.1144/SP328.1.

599 Reid, J., Plumley, P., and Schellekens, J. 1991. Paleomagnetic evidence for late miocene counterclockwise rotation  
600           of north coast carbonate sequence, Puerto Rico. *Geophysical Research Letters* 18: 565–568.

601 Schellart, W. P., Freeman, J., Stegman, D. R., Moresi, L., and May, D. 2007. Evolution and diversity of subduction  
602           zones controlled by slab width. *Nature* 446: 1–4. doi:10.1038/nature05615.

603 Shillington, D. J., Holbrook, W. S., Kelemen, P. B., and Hornbach, M. J. 2004. Composition and structure of the  
604           central Aleutian island aShillington, Donna J., Holbrook, W Steven., Kelemen, Peter B., and Hornbach,  
605           Matthew J. 2004. Composition and structure of the central Aleutian island arc from arc-parallel wide-angle  
606           seismic data. *Geochemistry, Geophysics, Geosystems* 5: 32. doi:10.1029/2004GC000715.

607 Smith, W. H. F., and Sandwell, D. T. 1997. Global Sea Floor Topography from Satellite Altimetry and Ship Depth  
608           Soundings. *Science* 277: 1956–1962.

609 Symithe, S., Calais, E., De Chabaliér, J. B., Robertson, R., and Higgins, M. 2015. Current Block Motions and  
610           Strain Accumulation on Active Faults in the Caribbean. *Journal of Geophysical Research*.

611 Syracuse, E. M., and Abers, G. A. 2006. Global compilation of variations in slab depth beneath arc volcanoes and  
612           implications. *Geochemistry, Geophysics, Geosystems* 7. Wiley Online Library.

613 White, R. S., Mckenzie, D. N., and Nions, K. O. 1992. Oceanic crustal thickness from seismic measurements and  
614           rare earth element inversions. *Journal of Geophysical Research* 97: 19,683-19,715.

615 Zelt, C. A., and Smith, R. B. 1992. Seismic traveltime inversion for 2 D crustal velocity structure. *Geophysical*  
616           *Journal International* 108: 16–34. doi:10.1111/j.1365-246X.1992.tb00836.x.

617

618

## 619 Supplementary data

### 620 Pre-processing and processing of multichannel seismic data

621 The quality control and the binning of the MCS data were performed on board using  
622 QCSispeed® (Antithesis 1) and SolidQC® (Antithesis 3) developed by Ifremer and the  
623 processing was performed using GEOCLUSTER® and GEOVATION®. The processing  
624 sequence includes: a 4 ms data sampling, a band-pass filtering (2-7-60-80 Hz), a FK filtering  
625 in order to reduce linear noises, amplitude attenuation for noisy traces due for example to  
626 streamer birds, a predictive deconvolution to improve the image resolution, velocity analysis  
627 and Normal Move-Out (NMO) correction, external mute to remove the direct and refracted  
628 waves and reduce the far offset reflection stretching, internal mute to reduce the primary  
629 multiple amplitude, velocity stack. As the acquisition is at deep water depth, we applied a post  
630 stack (f,k) migration at constant velocity of 1520 m/s.

### 631 Comparison between MCS and WAS lines

632 For modelling the AN1 velocity model, the sedimentary interfaces, the top of the crust and the  
633 interplate were interpreted from the reflection seismic profiles and converted in kilometers  
634 helping to build the model. For AN3 and AN5 models, MCS profiles were acquired during  
635 Antithesis 3, thus 2 years after wide-angle data. Thus, we simply checked that the velocity  
636 model interfaces is coincided with the interpretation of the following profiles (Figure a).

637

638

639

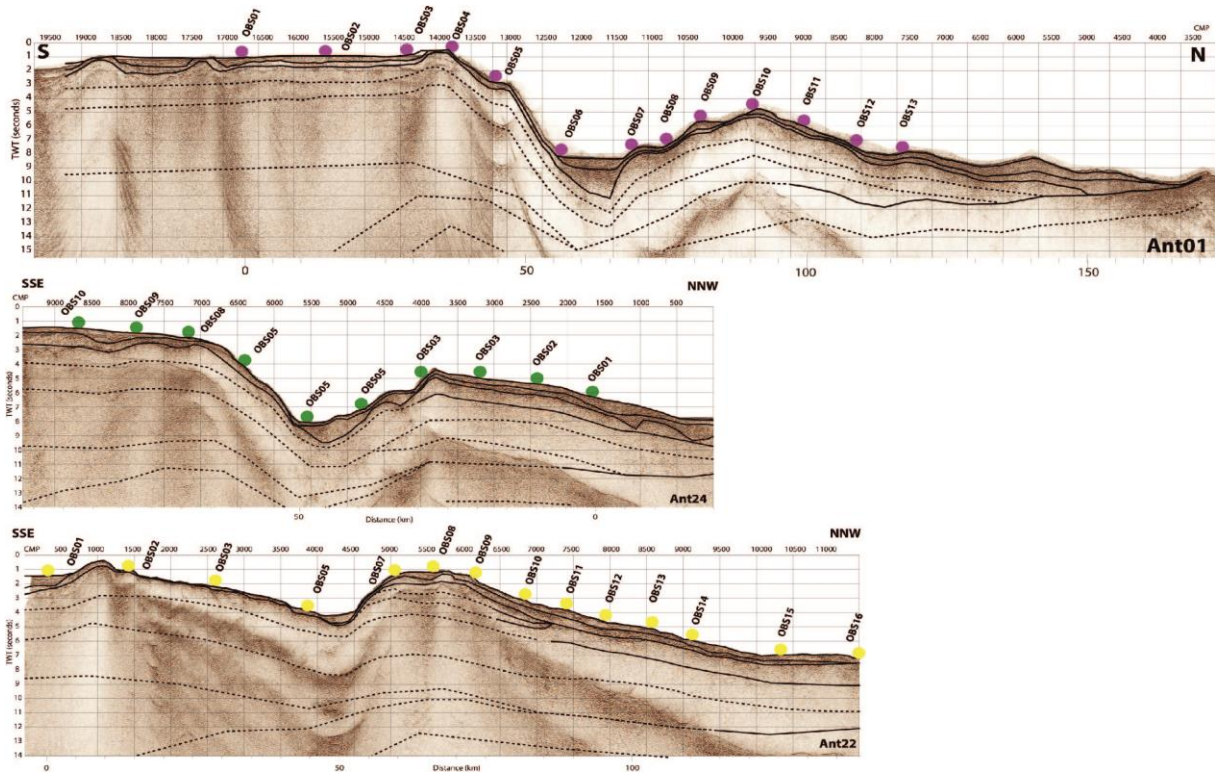


Figure a: Reflection seismic lines coincident with velocity model interfaces. The solid lines correspond in interfaces of the wide-angle model that were interpreted on seismic reflection data and the dotted line is only interfaces of the model In OBS locations are indicated by colored circles.

640

641 Resolution, RMS and  $\chi^2$

642 A total of 24419 points were modelled (Figure b) for a total of 28787 pointed arrivals, then  
 643 approximately 85% (Table 1).

644

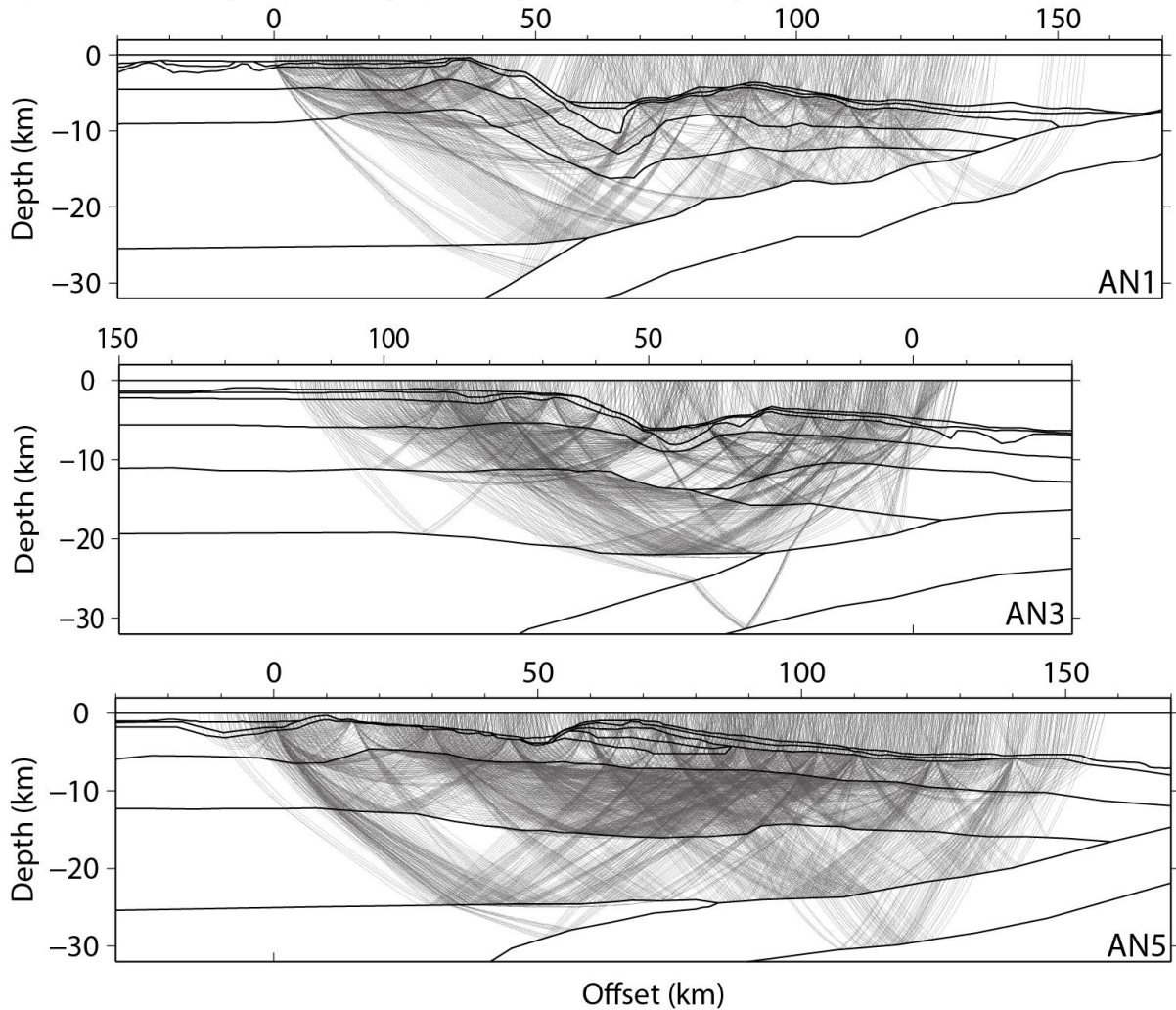
645

profile	number of modelised data	number of picked data	rate
AN1	6184	7788	79,40
AN3	6837	8340	81.98
AN5	11425	12659	90.25
total	24446	28787	84.92

646 Table 1 : number of picked travel times and number arrivals predicted from the three velocity models

647

648 *Figure b: 1 on 5 raypath for each profile are presented on each profile 1.*



649 The pointed phases depend on user and data quality. When the source-to-receiver distance  
 650 increases, the arrival phases are generally less accurate due to noise increasing. Indeed, for  
 651 larger offsets, it is easier to observe the first oscillation of the lower frequency bubble than the  
 652 first peak (high frequency). Thus, an uncertainty is proposed by the user for each phases pointed  
 653 according to its accuracy. This uncertainty can vary between 60 ms for the direct wave and 200  
 654 ms for larger offsets (Table 2).

655 We evaluate the resolution of velocity model by the root mean square error (RMS). For AN1  
 656 profile, the RMS error is 0.158 ms; for AN3; 0.167 ms and for AN5; 0.150 ms. This parameter  
 657 is also calculated for each phase, the RMS error value varies between 0.060 ms for the direct  
 658 wave and 0.291 ms for the deeper phases (Table 2).

659 Another value is calculated by the formula below, the  $\chi^2$ , which links the difference between  
 660 the observed and calculated arrival times, the number of pointed phases and the pointed  
 661 uncertainties (Table 2).

662

$$\chi^2 = \frac{1}{N} \sum_N^i \left( \frac{t_{calc}(i) - t_{obs}(i)}{\sigma(i)} \right)^2$$

663 With,

664  $N$  : calculated arrival number;  $t_{obs}(i)$  : pointed arrival times;  $t_{calc}(i)$  : calculated arrival times  
665 et  $\sigma(i)$  : pointed uncertainty.

666

667 The best constrained model corresponds to the lowest RMS, the highest modelled peak number  
668 and the  $\text{Chi}^2$  closest to 1 (Table 2).

669

AN1 Phases	Number of data	RMS (s)	Chi <sup>2</sup>	AN3 Phases	Number of data	RMS (s)	Chi <sup>2</sup>
Direct	603	0,084	1.974	Direct	622	0,57	0910
PS1	74	0,159	2.555	PS1	15	0,081	0.70
Ps1P	145	0,126	1.607	Ps1P	391	0,091	0.827
PS2	89	0,108	1.186	PS2	85	0,099	0.998
Ps2P	221	0,095	0.909	Ps2P	266	0,061	0.371
aPC1	1469	0,119	0.631	PC1	954	0,098	0.956
Pc1P	498	0,133	0.782	Pc1P	474	0,121	1.467
PC2	1042	0,182	1.482	PC2	1419	0,216	2.084
Pc2P	521	0,189	1.596	Pc2P	770	0,18	1.445
PC3	447	0,182	1.472	PC3	104	0,283	3.593
Pc3P	959	0,206	1.066	Pc3P	138	0,173	1.335
PcoP	50	0,204	1.065	PC4	697	0,261	3.023
PmP	66	0,205	1.071	Pc4P	761	0,122	0.372
Total	6184	0,158	1.196	Pn	88	0,176	0.780
				PcoP	0		
AN5 Phases	Number of data	RMS (s)	Chi <sup>2</sup>	PmP	53	0,092	0.216
Direct	518	0,053	0.795	Total	6837	0,166	1.429
PS1	83	0,073	0.412		Pointed phase uncertainty (s)	Glossary of seismic phases	
Ps1P	321	0,083	0.697	Direct	0.06	Direct wave through the water	
PS2	213	0,119	1.424	PSn	0.1	P-wave refracted phase through nth sedimentary layer	
Ps2P	230	0,073	0.536	PsnP	0.1	P-wave reflected phase from the bottom of the nth sedimentary layer	
PS3	92	0,170	2.934	Pcn	0.15	P-wave refracted phase through the crust layer	
Ps3P	25	0,078	0.630	PcnP	0.15	P-wave reflected phase from the bottom of the nth crust layer	
PS4	0	0	0	Pn	0.2	P-wave Moho refracted phase for the upper plate	
Ps4P	199	0,105	1.108	PcoP	0.2	P-wave reflected phase on the top of the subducting plate under the moho of the upper plate	
PC1	2021	0,110	0.536	PmP	0.2	P-wave Moho reflection on the bottom of the subduction plate	
Pc1P	779	0,105	0.493				
PC2	2961	0,138	0.845				
Pc2P	1807	0,158	1.109				
PC3	114	0,143	0.920				
Pc3P	1492	0,225	1.262				
Pn	289	0,261	1.703				
PcoP	54	0,163	0.677				
PmP	227	0,163	1.358				
Total	11425	0,150	0.909				

670 *Table 2 : Residual travel times for all reflected and refracted phases for AN1-AN3 and AN5 transect,*  
671 *using forward modeling (Zelt and Smith 1992)*

672

673 OBS sections

674 The following figures show, for each panel, (A) Ray coverage every fifth ray plotted. (B)  
675 Observed travel times (colored bars) according to phases picks and calculated travel time (solid  
676 lines). (C) OBS seismic section with picked phases (D) Uninterpreted OBS seismic section.

677

678

